Inorganic Chemistry

pubs.acs.org/IC Article

Exploring the In Vivo and In Vitro Anticancer Activity of Rhenium Isonitrile Complexes

Sierra C. Marker,[‡] A. Paden King,[‡] Samantha Granja, Brett Vaughn, Joshua J. Woods, Eszter Boros, and Justin J. Wilson*

Cite This: *Inorg. Chem.* 2020, 59, 10285−10303 Read Online

ACCESS | Metrics & More | Article Recommendations | Supporting Information

ABSTRACT: The established platinum-based drugs form covalent DNA adducts to elicit their cytotoxic response. Although they are widely employed, these agents cause toxic side-effects and are susceptible to cancer-resistance mechanisms. To overcome these limitations, alternative metal complexes containing the rhenium(I) tricarbonyl core have been explored as anticancer agents. Based on a previous study (*Chem. Eur. J.* 2019, *25*, 9206), a series of highly active tricarbonyl rhenium isonitrile polypyridyl (TRIP) complexes of the general formula *fac*-$[Re(CO)_3(NN)(ICN)]^+$, where NN is a chelating diimine and ICN is an isonitrile ligand, that induce endoplasmic reticulum (ER) stress via activation of the unfolded protein response (UPR) pathway are investigated. A total of 11 of these TRIP complexes were synthesized, modifying both the equatorial polypyridyl and axial isonitrile ligands. Complexes with more electron-donating equatorial ligands were found to have greater anticancer activity, whereas the axial ICN ligands had a smaller effect on their overall potency. All 11 TRIP derivatives trigger a similar phenotype that is characterized by their abilities to induce ER stress and activate the UPR. Lastly, we explored the in vivo efficacy of one of the most potent complexes, *fac*-$[Re(CO)_3(dmphen)(ptolICN)]^+$ (**TRIP-1a**), where dmphen = 2,9-dimethyl-1,10-phenanthroline and *p*tolICN = *para*-tolyl isonitrile, in mice. The ^{99m}Tc congener of **TRIP-1a** was synthesized, and its biodistribution in BALB/c mice was investigated in comparison to the parent Re complex. The results illustrate that both complexes have similar biodistribution patterns, suggesting that ^{99m}Tc analogues of these TRIP complexes can be used as diagnostic partner agents. The in vivo antitumor activity of **TRIP-1a** was then investigated in NSG mice bearing A2780 ovarian cancer xenografts. When administered at a dose of 20 mg/kg twice weekly, this complex was able to inhibit tumor growth and prolong mouse survival by 150% compared to the vehicle control cohort.

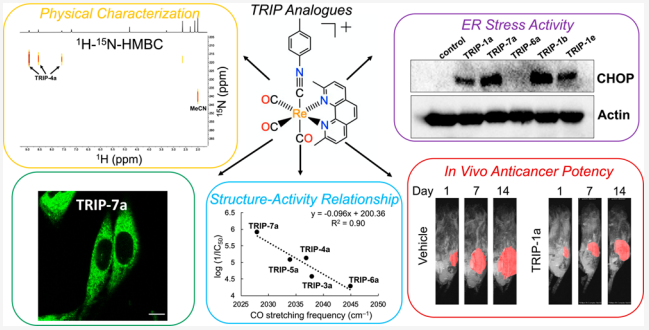

INTRODUCTION

Platinum-based drugs are currently employed in approximately 50% of all cancer treatment regimens.[1] Despite their widespread use, these drugs have significant drawbacks that limit their efficacy. These drawbacks arise from their acute and chronic side-effects and the tendency of cancer cells to develop resistance to them.[2−5] To overcome these limitations, the development of new drugs with mechanisms of action distinct from the platinum-based anticancer agents has been pursued extensively. One relatively new promising class of anticancer agents comprises compounds that target endoplasmic reticulum (ER) stress pathways.[6−9] Cancer cells and tumors often exhibit heightened levels of ER stress compared to normal cells because of their increased burden of reactive oxygen species (ROS) and higher rates of protein misfolding.[10−12] To compensate for this stress, cancer cells will upregulate the unfolded protein response (UPR) pathway, which helps manage protein homeostasis. This upregulation renders cancer cells sensitive to compounds that induce ER stress,[13−16] leading to apoptosis, autophagy, or paraptosis.[17−20] The strategy of targeting the UPR and triggering ER stress is highlighted by the clinical approval of the anticancer agents bortezomib and carfilzomib, which cause ER stress by inhibiting the proteasome.[21]

Based on the success of these proteasome inhibitors, which validate ER stress as a strategy for cancer therapy, there has been a surge of interest in ER-targeted anticancer agents in recent years. Among these compounds, organometallic and coordination complexes of Ru,[22−25] Au,[26−28] Ir,[29−34] Os,[35,36] and Pt[37,38] have arisen as particularly promising candidates. Complexes of these metal ions often exhibit intrinsic ER localization due to their positive charges and hydrophobicity, making them outstanding candidates for ER stress-inducing

Received: May 16, 2020
Published: July 7, 2020

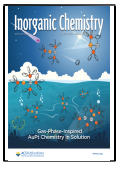

https://dx.doi.org/10.1021/acs.inorgchem.0c01442
Inorg. Chem. 2020, 59, 10285−10303

Chart 1. TRIP Complexes Explored in This Study

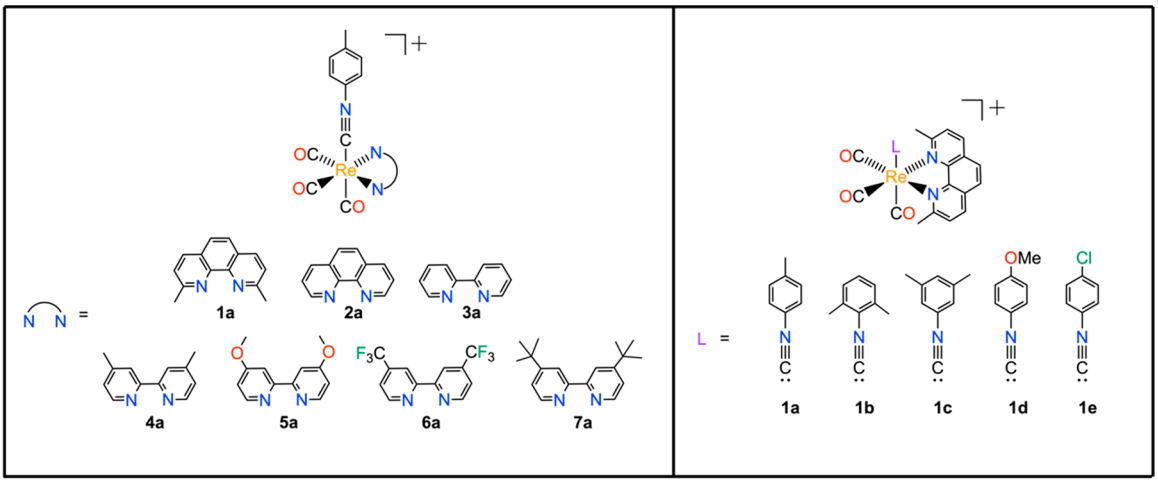

therapeutics. These metal-based agents operate via a wide range of mechanisms, including disruption of intracellular Ca^{2+} trafficking, inhibition of thioredoxin reductases, and photoactivated generation of ROS. The broad mechanistic range and potent anticancer activity of these compounds demonstrates the potential of inorganic and organometallic complexes as ER stress-inducing anticancer agents.

We and others have been investigating rhenium complexes as alternatives to conventional platinum-based drugs.[39−64] During the course of these studies,[65−69] we discovered a tricarbonyl rhenium isonitrile polypyridyl complex, $[Re(CO)_3(dmphen)(ptolICN)]^+$ (**TRIP-1a**), where dmphen = 2,9-dimethyl-1,10-phenanthroline and *p*tolICN = *para*-tolyl isonitrile, which has potent anticancer activity in a wide range of cancer cells.[69] This complex induces apoptosis by increasing the unfolded protein burden and triggering ER stress. Furthermore, we have used X-ray fluorescence (XRF) microscopy to verify that these complexes are highly stable in cells,[70] and we have developed an ovarian cancer cell line that is resistant to TRIP, which is a consequence of enhanced expression of drug efflux transporters and metallothioneins by these cells.[71]

Though our previous experiments have thoroughly characterized the biological activity of TRIP, our current understanding of these complexes could be furthered significantly by exploring new derivatives. To better understand **TRIP-1a**, we designed a small library of related rhenium tricarbonyl complexes bearing various equatorial polypyridyl and axial isonitrile ligands in order to probe structure−activity relationships (SARs) for this compound class. In this study, we describe the synthesis and characterization of 10 new analogues of **TRIP-1a** and an evaluation of their anticancer activities and ER stress-inducing properties. Through these studies, we have found that complexes with more hydrophobic and electron-donating ligands have higher cytotoxicities. Furthermore, we describe in vivo studies that elucidate the biodistribution of **TRIP-1a** and its ^{99m}Tc analogue, as well as its anticancer activity in an ovarian cancer xenograft model. Collectively, this study demonstrates the viability of TRIP complexes as a new class of metal-based ER stress-inducing agents with promising in vitro and in vivo anticancer properties.

RESULTS AND DISCUSSION

Library Design. The modular coordination environment of the TRIP complexes makes them amenable for making systematic modifications to tune their properties. Both the hydrophobicity and electron-donating properties of the TRIP ligands alter the biological and physical properties of these complexes. To assess the role of the ligands on these attributes, we designed a library to modify both the equatorial polypyridyl and the axial isonitrile ligands. We chose the equatorial ligands dmphen (**1**), 1,10-phenanthroline (**2**), 2,2′-bipyridine (**3**), 4,4′-dimethyl-2,2′-bipyridine (**4**), 4,4′-dimethoxy-2,2′-bipyridine (**5**), 4,4′-bis(trifluoromethyl)-2,2′-bipyridine (**6**), and 4,4′-di-*tert*-butyl-2,2′-bipyridine (**7**) based on their different steric, hydrophobic, and electronic properties. These equatorial ligands were paired with the *para*-tolyl isonitrile (ICN) axial ligand **a** to obtain the seven complexes **TRIP-1a**, **TRIP-2a**, **TRIP-3a**, **TRIP-4a**, **TRIP-5a**, **TRIP-6a**, and **TRIP-7a** (Chart 1). To probe the role of the ICN ligand, we prepared another series of TRIP complexes that keep the polypyridyl ligand constant (**1**), while varying the axial ligand through addition of either *para*-tolyl ICN (**a**), 2,6-dimethylphenyl ICN (**b**), 3,5-dimethylphenyl ICN (**c**), *para*-methoxyphenyl ICN (**d**), or *para*-chlorophenyl ICN (**e**). Thus, an additional four TRIP complexes, **TRIP-1b**, **TRIP-1c**, **TRIP-1d**, and **TRIP-1e**, comprise this subset of the library. A total of 11 complexes was incorporated into our full complex library (Chart 1).

These TRIP complexes were synthesized using a modification of a previously reported procedure.[69] Briefly, *fac*-$[Re(CO)_3(NN)Cl]$, where NN = polypyridyl ligand, was heated under reflux with 1 equiv of AgOTf (OTf = trifluoromethanesulfonate) in dry tetrahydrofuran (THF) for 3 h to abstract the chloride ligand. Solid AgCl was removed by filtration, and an excess (4 equiv) of the desired ICN ligand was added. After refluxing overnight, the products were isolated in moderate yields and purified either by repeated recrystallization or column chromatography. The products were yellow to off-white powders, with more strongly donating equatorial ligands giving rise to whiter products. These 11 complexes were characterized by ^1H NMR spectroscopy (Figures S1−S10), high-resolution electrospray ionization mass spectrometry (HR-ESI-MS), and Fourier-transform infrared (FTIR) spectroscopy (Figures S11−S20), and their purities were verified with high-performance liquid chromatog-

https://dx.doi.org/10.1021/acs.inorgchem.0c01442
Inorg. Chem. 2020, 59, 10285−10303

raphy (HPLC, Figures S21−S30) and elemental analysis. The products are extremely stable. They may be stored indefinitely in the dark at room temperature, and previous studies have indicated that **TRIP-1a** exhibits no measurable degradation after a week in aqueous solution, even in the presence of glutathione.[69]

Physical Characterization. The physical properties of the complexes were evaluated using several techniques, including FTIR spectroscopy, single-crystal X-ray diffraction (XRD), cyclic voltammetry (CV), and $^{1}H-^{15}N$-HMBC (heteronuclear multiple bond correlation) NMR spectroscopy. Within the IR spectra, 3 C≡O stretching modes are expected because of the C_s symmetry of these complexes. In some cases, the two lower-energy stretching modes overlap and are unresolved. Additionally, a diagnostic C≡N stretching mode in the energy range of 2155−2186 cm^{-1} was also detected, confirming the incorporation of this axial ligand. In comparing **TRIP-1a**−**TRIP-1e**, complexes which all bear the same equatorial dmphen ligand but different ICNs, the 3 C≡O stretching frequencies are relatively invariant and span a narrow range of 2033−2036, 1957−1967, and 1926−1941 cm^{-1}. The C≡N stretching frequency, however, does predictably change depending on the type of substituents that are present on the ICN ligand. ICN ligands with more electron-donating substituents give rise to lower-energy C≡N stretches than those with less electron-donating groups. For example, the C≡N stretching frequency for **TRIP-1d**, which bears an electron-donating *p*-methoxy ICN, is found at 2179 cm^{-1}, whereas for **TRIP-1e** with an electron-withdrawing *p*-chloro ICN, this mode occurs at 2185 cm^{-1}. A notable outlier in this series is that of **TRIP-2a**. For this complex, the C≡N stretch occurs at a 2155 cm^{-1}, an energy that is significantly lower than that of the other complexes. Structural data, obtained via X-ray crystallography (vide infra), indicate that the ICN ligand has a pronounced bend in this complex, providing a rationale for the lower energy C≡N stretch in **TRIP-2a**. As the equatorial ligand is varied over **TRIP-1a**−**TRIP-7a**, however, changes in the energy of the C≡O stretching modes are apparent with more electron-donating ligands giving rise to lower energy vibrations. This trend is most apparent for complexes **TRIP-3a**−**TRIP-6a**, which all contain derivatives of the 2,2′-bipyridine (bpy) ligand. For instance, **TRIP-6a**, which bears the electron-deficient 4,4′-bis(trifluoromethyl)-2,2′-bipyridine ligand, has relatively high-energy C≡O stretching frequencies at 2045, 1976, and 1944 cm^{-1}, whereas **TRIP-7a**, with the strongly electron-donating 4,4′-di-*tert*-butyl-2,2′ bipyridine ligand, exhibits lower-energy C≡O stretching frequencies at 2028, 1959, and 1931 cm^{-1}. For these complexes, more electron-donating ligands give rise to more electron-rich metal centers that engage in more extensive π-back-bonding with the CO ligands, resulting in a weaker C≡O bond. As shown by the relative lack of variability in the C≡O stretching frequencies of complexes **TRIP-1a**−**TRIP-1e**, the equatorial polypyridyl ligand has a larger effect on the electron-richness of the metal center than the ICN axial ligand.

Single crystals of **TRIP-2a**, suitable for XRD analysis, were grown by diffusion of diethyl ether into a dichloromethane (DCM) solution. Crystallographic refinement and data collection parameters and relevant interatomic distances and angles are reported in Tables S1 and S2, respectively. The structural metrics of this complex are generally comparable to those of **TRIP-1a** and other related rhenium tricarbonyl isonitrile structures.[69,72−76] A key difference between these structures, however, is the Re−C4−N3 bond angle of the ICN. This angle in **TRIP-2a** is noticeably bent at 169.4(3)° (Figure 1a). By contrast, the same angle in **TRIP-1a** is close to being

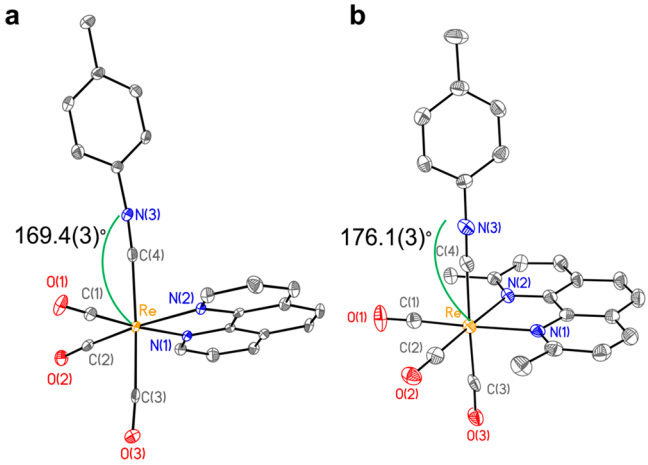

Figure 1. (a) X-ray crystal structure of **TRIP-2a**. The Re−C4−N3 interatomic angle is 169.4(3)° and the C4−N3 distance is 1.132(4) Å. Selected interatomic distances: Re−C(1), 1.944(3); Re−C(2), 1.933(3); Re−C(3), 1.986(3); Re−C(4), 2.081(3); Re−N(1), 2.183(2); Re−N(2), 2.137(2). (b) X-ray crystal structure of **TRIP-1a** taken from ref 69. Selected interatomic distances: Re−C(1), 1.908(4); Re−C(2), 1.931(4); Re−C(3), 1.960(4); Re−C(4), 2.083(4); Re−N(1), 2.221(3); Re−N(2), 2.216(3). Ellipsoids are drawn at 50% probability. Hydrogen atoms and counterions are omitted for clarity.

linear at 176.1(3)° (Figure 1b),[69] consistent with other reported rhenium isonitrile complexes, which have bond angles ranging from 173.6(3) to 176.1(3)°. The deviation from linearity in **TRIP-2a** may be a consequence of increased back-bonding from the Re center to the ICN ligand. This type of interaction populates the π^* orbital of the ICN ligand, leading to an effective decrease in C≡N bond order and a shift in hybridization of the carbon atom closer to sp^2. As noted above, this hypothesis is supported by the significantly lower-energy C≡N stretching frequency of 2155 cm^{-1} for **TRIP-2a** relative to the other derivatives, which exhibit C≡N stretching frequencies between 2171 and 2186 cm^{-1}. The C≡N stretching frequencies for two previously reported and crystallographically characterized rhenium isonitrile complexes, *fac*-[Re(CO)$_3$(1,10-phenanthroline)(*ortho*-methoxyphenylICN)]PF_6 and *fac*-[Re(CO)$_3$(bpy)(2,6-dimethylphenylICN)]OTf, are 2173 and 2181 cm^{-1}, respectively. These two structures show only moderate deviations from linearity with $Re-C_{ICN}-N_{ICN}$ bond angles of 175.8(3) and 173.6(3)°, respectively.[72,75] However, for more electron-rich, low-valent first row transition metal complexes, the bending of the ICN ligands can give rise to angles of less than 135°,[77,78] indicating that the effects observed for **TRIP-2a** are relatively modest.

To probe the electronic properties of these complexes, we employed $^{1}H-^{15}N$-HMBC NMR spectroscopy. Although the low gyromagnetic ratio and 0.37% natural abundance of ^{15}N makes it difficult to detect directly in unenriched samples, magnetization transfer from other nuclei, such as ^{1}H, can allow for signal enhancement via 2D NMR spectroscopic methods including HMBC.[79] Heteronuclear NMR spectroscopy is especially useful for analyzing metal-based anticancer agents

https://dx.doi.org/10.1021/acs.inorgchem.0c01442
Inorg. Chem. 2020, 59, 10285−10303

Table 1. Physical Properties of TRIP Derivatives

compound	^{15}N chemical shift (ppm)[a,b]	E_{pc} (V vs SCE)	λ, nm (ε, M^{-1} cm^{-1})	λ, nm (Φ, %)	τ (μs)	τ_{N2}[d] (μs)
TRIP-1a	223.7	−1.25	230 (39900 ± 2000), 261 (44800 ± 2200), 282 (33800 ± 1600), 306 (21000 ± 900), 369 (2000 ± 100)[c]	505 (3.1 ± 0.3)[c]	1.1[c]	3.5
TRIP-2a	222.3	−1.18	270 (46600 ± 1200), 301 (16200 ± 300), 364 (3000 ± 100)	512 (5.3 ± 0.4)	1.8	10.9
TRIP-3a	225.8	−1.18	244 (31000 ± 700), 260 (39100 ± 1800), 306 (17200 ± 700), 317 (16500 ± 1400), 332 (6100 ± 400)	523 (6.3 ± 0.2)	0.7	1.0
TRIP-4a	217.6	−1.30	244 (34400 ± 700), 261 (43200 ± 900), 303 (18600 ± 400), 314 (18400 ± 400), 333 (6800 ± 200)	516 (6.7 ± 0.1)	0.8	1.3
TRIP-5a	201.8	−1.33	223 (33900 ± 2100), 260 (41200 ± 2500), 303 (14100 ± 800), 332 (6600 ± 400)	525 (3.9 ± 0.3)	0.4	0.7
TRIP-6a	236.8	−0.75	260 (35600 ± 1700), 297 (17800 ± 600), 324 (11900 ± 700), 365 (3800 ± 100)	584 (0.8 ± 0.1)	0.1	0.1
TRIP-7a	n.d.	−1.30	260 (44200 ± 1200), 304 (19800 ± 100), 315 (18800 ± 900), 334 (7300 ± 100)	518 (7.7 ± 0.2)	0.7	1.6
TRIP-1b	n.d.	−1.28	259 (39100 ± 1600), 283 (31200 ± 1200), 305 (19400 ± 900), 370 (2000 ± 300)	503 (2.7 ± 0.3)	1.2	6.8
TRIP-1c	n.d.	−1.27	261 (36100 ± 800), 283 (29600 ± 500), 305 (18900 ± 800), 367 (2500 ± 60)	504 (1.6 ± 0.1)	1.1	5.3
TRIP-1d	n.d.	−1.26	268 (58200 ± 1700), 283 (46700 ± 1700), 306 (27900 ± 900), 2369 (600 ± 300)	506 (2.8 ± 0.3)	1.0	4.0
TRIP-1e	n.d.	−1.29	264 (44400 ± 2300), 284 (34600 ± 1700), 305 (21400 ± 1200), 369 (2000 ± 30)	501 (2.3 ± 0.1)	1.3	5.6

[a]n.d. = not determined. [b]Referenced to the internal standard acetonitrile at 240 ppm vs liquid NH_3 at 0 ppm. [c]Reported in ref 69. [d]Luminescence lifetime measured in nitrogen-saturated PBS (pH 7.4).

because NMR-active nuclei, such as ^{15}N and ^{31}P, are often directly bound to the metal center of interest.[80] On the basis of this precedence, we used ^{1}H−^{15}N HMBC NMR spectroscopy to determine the ^{15}N chemical shifts of **TRIP-3a**−**TRIP-7a**, the complexes bearing bpy ligands. The ^{15}N chemical shifts of the bpy nitrogen atoms of these complexes span approximately 40 ppm, beginning at 202 ppm for **TRIP-5a** and ranging up to 237 ppm for **TRIP-6a** (Table 1 and Figures S31−S36). These shifts are comparable to those previously reported for the ^{15}N nuclei within bpy and 1,10-phenathroline (phen) ligands that are present within a series of Pd(II) and Pt(II) complexes. The ^{15}N chemical shifts for these complexes also hover around 200 ppm, ranging from 203 to 218 ppm and 201 to 216 ppm for Pd and Pt, respectively.[81] These ^{15}N chemical shifts are related to the electron-donating properties of the equatorial ligands. Stronger donors, like 4,4′-dimethoxy-2,2′-bipyridine in **TRIP-5a**, give rise to more upfield shifts, and weaker donors, like 4,4′-bis(trifluoromethyl)-2,2′-bipyridine in **TRIP-6a**, give rise to downfield shifts. Although in principle detecting the ^{15}N resonance of the ICN ligands should be possible as well, we generally found this signal to be undetectable within a time span of less than 4 h. Only for a highly concentrated sample of **TRIP-4a** were we able to observe a ^{15}N, ^{1}H crosspeak resonating at 175 ppm in the ^{15}N channel. Although we could not reliably measure the ^{15}N resonance of the isonitrile ligands, our data for the equatorial bpy ligands indicates that these chemical shifts can be used as a reporter of the electronic properties of these complexes.

Because redox processes often play a critical role in mediating the anticancer activities of metal-based drug candidates,[82,83] the electrochemical properties of the TRIP compounds were investigated using cyclic voltammetry (CV) in acetonitrile (Table 1 and Figures S37−S47). The cyclic voltammograms of these complexes all display a prominent irreversible reduction peak at potentials spanning −0.75 to −1.33 V vs SCE. Given prior electrochemical studies of rhenium tricarbonyl complexes with polypyridyl and isonitrile ligands, these peaks in the voltammograms are assigned to ligand-based reductions.[84] Notably, all of these reduction events occur at potentials that are outside of the biologically relevant range. However, the values of these reduction potentials can be used as a readout on the electronic properties of these complexes. These potentials correlate, as expected, with the electron-donating properties of the diimine ligands. For example, **TRIP-6a**, which bears the most electron-deficient polypyridyl ligand, has the most positive reduction potential. The redox potentials for **TRIP-3a**−**TRIP-6a** also correlate with the ^{15}N chemical shifts of the diimine ligands with an R^2 value of 0.71 (Figure S48). This correlation reflects the fact that both parameters provide a complementary measure for the electron-donating strengths of the diimine ligands.

Because rhenium tricarbonyl complexes have been extensively used as cellular imaging agents,[85,86] we investigated the photophysical properties of these TRIP complexes to assess their suitability for this application. The absorbance (Figures S49−S58) and emission (Figures S59−S68) spectra for all complexes were collected in phosphate-buffered saline (PBS, pH 7.4) containing ≤1% DMSO (Table 1). The absorbance and emission profiles of **TRIP-1a**−**TRIP-1e**, complexes containing the same dmphen equatorial ligand but different axial ICN ligands, are all nearly identical with only small differences in emission quantum yields and lifetimes. By contrast, when the equatorial ligands are varied across **TRIP-1a**−**TRIP-7a**, significant differences in the absorbance and emission energies are observed. As the equatorial polypyridyl ligands become more electron-deficient, the lowest-energy absorbance maxima, which are attributed to metal-to-ligand charge transfer (MLCT) transitions, undergo a red-shift. Likewise, the emission of these complexes, which is attributed to a relaxation of the ^{3}MLCT excited state, also undergoes a red-shift as the ligands contain more electron-withdrawing substituents. For instance, the emission maximum of **TRIP-6a**, with the electron-withdrawing 4,4′-bis(trifluoromethyl)-2,2′-bipyridine ligand, is at 584 nm, whereas for **TRIP-5a**, which

https://dx.doi.org/10.1021/acs.inorgchem.0c01442
Inorg. Chem. 2020, 59, 10285−10303

bears the donating 4,4′-dimethoxy-2,2′-bipyridine ligand, this maximum occurs at 525 nm. Both the lack of effect of the axial ICN ligands and the importance of electron-withdrawing substituents on the equatorial ligands are consistent with the MLCT nature of these excited states in which the accepting ligand π^* orbital resides solely on the diimine.[87] However, for related complexes with large aromatic ICN axial ligands, MLCT states featuring these ligands are accessible.[87]

The emission quantum yields (Φ), measured relative to quinine sulfate as a standard, range from 1% to 8% in air-equilibrated PBS. As expected, these values are generally correlated to the energy of the excited state, following the well-known energy-gap law.[88] **TRIP-6a**, for example, has the lowest quantum yield (0.8%), which coincides with it also having the lowest-energy absorbance and emission energies in the series. The emission quantum yields are generally higher for complexes containing derivatives of bpy (**TRIP-3a**−**TRIP-7a**) compared to those that contain derivatives of phen, which is somewhat surprising in the context of the energy-gap law because the phen ligands have higher-energy emission maxima. The luminescence lifetimes of the complexes (Figures S69−S78) range from 0.1 to 2 μs in air-equilibrated PBS. Furthermore, these lifetimes increase by a factor of 1.5−5 in an atmosphere of N_2. These results provide further confirmation that the emission arises from an O_2-sensitive ^{3}MLCT excited state. In general, the complexes containing derivatives of phen as equatorial ligands (**TRIP-1a**−**1e** and **TRIP-2a**) exhibit much larger changes in their luminescence lifetimes in response to the presence of O_2, which may also account for their lower Φ in air-equilibrated buffer compared to the bpy derivatives. The relatively high emission quantum yields of these complexes in aqueous buffer suggest that they could be valuable for various biological imaging applications. The photophysical properties for several other series of Re polypyridyl complexes bearing ICN ligands have been previously reported.[72,84,89] These prior studies reveal trends similar to what we observed here for the TRIP complexes. Specifically, greater donating-capacity of the equatorial ligand results in a blue-shift in the emission maxima, electron-deficient equatorial ligands decrease the emission quantum yields, and the axial ICN ligand has little effect on the emissive properties of the complexes.[72,84,89]

Anticancer Activity and Intracellular Luminescence. With the physical properties of the TRIP complexes thoroughly investigated, we next sought to evaluate their in vitro anticancer activities. The cytotoxicities of all 11 complexes in HeLa cells were tested with the colorimetric 3-(4,5-dimethylthiazol-2-yl)-2,5-tetrazolium bromide (MTT) assay. We chose to investigate HeLa cells because they are one of the most common models for initial investigation of chemotherapeutics, and they are an extremely well-characterized cell line. Furthermore, the original lead compound, **TRIP-1a**, exhibited potent cytotoxicity toward HeLa cells in our previous studies. The concentration required to inhibit 50% of the cell population (IC_{50} value) was determined for all of the TRIP derivatives (Table 2 and Figures S79−S88). The IC_{50} values of these complexes range from 1.2 to 53 μM, demonstrating that this class of complexes is cytotoxic. The relative activities of these complexes appear to be related to the electron-donating properties of the polypyridyl ligand. For example, **TRIP-6a**, which contains the weakly donating 4,4′-bis(trifluoromethyl)-2,2′-bipyridine ligand, is the least active complex with an IC_{50} value of 53 μM (Figure S83). The more electron-rich **TRIP-5a**, on the other hand, has a much lower IC_{50} value of 8.4 μM (Figure S82).

Table 2. IC_{50} Values of TRIP Derivatives and Cisplatin in HeLa Cells

compound	IC_{50} (μM)
TRIP-1a[a]	1.4 ± 0.2
TRIP-2a	5.8 ± 0.5
TRIP-3a	27.5 ± 0.6
TRIP-4a	7.6 ± 0.3
TRIP-5a	8.4 ± 1.9
TRIP-6a	53.1 ± 1.6
TRIP-7a	1.2 ± 0.5
TRIP-1b	1.8 ± 0.1
TRIP-1c	6.8 ± 0.1
TRIP-1d	5.0 ± 1.5
TRIP-1e	9.3 ± 3.7
cisplatin[a]	6.6 ± 0.7

[a]Reported in ref 69.

As discussed above, the C≡O stretching frequencies and ^{15}N chemical shifts of these complexes also correlate with the electron-donating strengths of the equatorial ligands. As such, it is reasonable that these parameters may serve as predictors of potency of these compounds. Figure 2a shows a plot of the ^{15}N chemical shifts versus $\log(1/IC_{50})$ for the complexes that contain bpy-ligand derivatives, **TRIP-3a**−**TRIP-7a**. If **TRIP-7a** is excluded as an outlier, a linear correlation ($R^2 = 0.77$) shows that complexes with upfield ^{15}N chemical shifts, like **TRIP-5a**, exhibit higher potency against HeLa cells. The need to remove **TRIP-7a** from this trend may be a consequence of its unusual steric profile compared to other compounds in this series. Correlations between ^{13}C NMR chemical shifts and biological activities of compounds is a surprisingly common phenomenon.[90] The trend involving the ^{15}N NMR chemical shifts observed within the TRIP series shows that these types of relationships may also apply to other nuclei. A similar plot of the highest-energy C≡O stretching frequency versus $\log(1/IC_{50})$ for complexes bearing bpy-ligand derivatives, **TRIP-3a**−**TRIP-7a**, also yields a clear linear correlation with $R^2 = 0.90$ (Figure 2b). These two correlations illustrate how experimentally measured physical properties can be used in a predictive sense for determining the anticancer potential of this class of compounds. More specifically, these trends show that more electron-rich TRIP complexes, a property that can be quantified by key IR and NMR spectroscopic signatures, exhibit higher cytotoxicity toward HeLa cells. Although these correlations use only the bpy-based TRIP complexes ($n = 5$ for both plots), the observed trends indicate that the activities of this class of compounds may be predicted on the basis of their physical properties.

To analyze the role of the ICN ligand, we can compare the activities of complexes **TRIP-1a**−**TRIP-1e**, which contain the same equatorial dmphen ligand, but different axial ligands. Overall, the nature of the ICN ligands has a smaller effect on the cytotoxicity of the compounds, as evidenced by the smaller range of IC_{50} values that span from 1.4 to 9.3 μM. Upon analysis of the different physical properties of these complexes, it is apparent that these activities, $\log(1/IC_{50})$, correlate with the C≡N stretching frequencies, as shown in Figure 2c. Complexes with greater C≡N stretching energies exhibit lower cytotoxicity. As noted above, the relative energies of the C≡N stretching frequencies themselves are related to the presence of

https://dx.doi.org/10.1021/acs.inorgchem.0c01442
Inorg. Chem. 2020, 59, 10285−10303

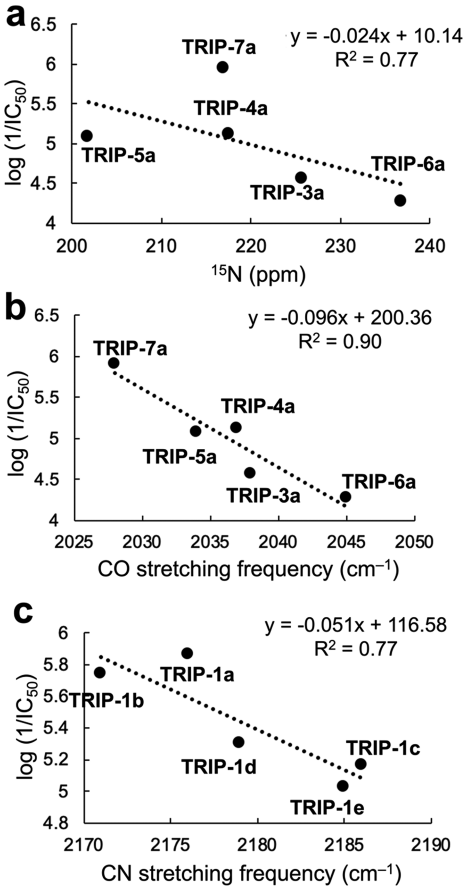

Figure 2. (a) Correlation of ^{15}N chemical shift (ppm) vs the log(1/IC_{50}) values in HeLa cells of the bpy-derived TRIP complexes (**TRIP-3a**−**TRIP-6a**), excluding **TRIP-7a** in the linear regression. (b) Correlation of the highest C≡O stretching frequency (cm^{-1}) vs the log(1/IC_{50}) values in HeLa cells of the bpy-derived TRIP complexes (**TRIP-3a**−**TRIP-7a**). (c) Correlation of the C≡N stretching frequency (cm^{-1}) vs the log(1/IC_{50}) values in HeLa cells of the dmphen-bearing TRIP complexes (**TRIP-1a**−**TRIP-1e**). The log(1/IC_{50}) values were determined using the IC_{50} values in units of M.

electron-donating or -withdrawing groups on the ICN ligand. Thus, it appears that more electron-rich complexes give rise to enhanced cytotoxicity.

In addition to electronic effects, sterics and lipophilicity also appear to play a role in mediating the cytotoxic activities of the complexes. For example, **TRIP-7a**, which bears a bulky and lipophilic 4,4′-di-*tert*-butyl-2,2′-bipyridine, is more active than **TRIP-5a**, which bears a diimine of equal electron-donating capabilities. Considering these results, we investigated potential correlations between the lipophilicities of the complexes, which are typically quantified by their partition (P) between octanol and water, and their activities. The log P values of the polypyridyl and isonitrile ligands were calculated separately using ALOGPS 2.1 software,[91,92] which is only parametrized to determine these values for organic compounds. We took the sum of these ligand log P values to quantitatively gauge the relative lipophilicities of each complex (Table S3).[93] A plot of the calculated log P values versus the compound activity is provided in Figure S89. Based on this analysis, there was a poor correlation between toxicity and calculated log P, indicating that other factors dictate the toxicities of the complexes.

Surprisingly, none of these TRIP derivatives exhibited significantly greater activity than the parent complex, **TRIP-1a**, which has an IC_{50} value of 1.4 μM in HeLa cells. Notably, we have previously identified the complex *fac*-[Re(CO)$_3$(dmphen)(OH$_2$)]$^+$ to be more active than related rhenium tricarbonyl complexes bearing axial water ligands.[65] Thus, the use of this diimine ligand with rhenium tricarbonyl complexes appears to give rise to favorable anticancer properties.

In addition to testing the in vitro anticancer activity of the TRIP derivatives, we explored their intracellular luminescence properties via confocal fluorescence microscopy. The reasonably high aqueous emission quantum yields and long lifetimes of rhenium tricarbonyl compounds make them useful agents for biological imaging, enabling their intracellular localization to be tracked.[85,86,94,95] Confocal fluorescence microscopy experiments were performed on HeLa cells treated with 10 μM of the TRIP derivatives for 2 h. The total emission intensity emanating from the cells was quantified to investigate the distribution and uptake of the TRIP complexes. With the exception of **TRIP-7a**, all of the complexes gave rise to intracellular luminescence intensities that were 3−8 times that of the autofluorescence of the untreated control (Figure S90). Notably, cells treated with **TRIP-7a** were approximately 16 times brighter than the untreated control. As shown in Table 1, **TRIP-7a** has the largest emission quantum yield of the series, a property that may account for its high intracellular luminescence signal. However, other factors, such as cellular uptake and environmental sensitivity of photophysical properties, also likely play a role in mediating the bright intracellular photoluminescence of these compounds. In comparing the fluorescence microscopy images, it is apparent that the complexes have different intracellular localization patterns. For instance, the photoluminescence of **TRIP-1a** and **TRIP-1e** is primarily localized around the nucleus in a punctate pattern. By contrast, **TRIP-7a** and **TRIP-1c** are distributed evenly throughout the cytoplasm. Interestingly, none of the complexes appear to localize to the nucleus. This result may indicate that these complexes do not target the nucleus. However, caution should be exercised in interpreting localization of these compounds based on fluorescence microscopy because the photoluminescence of the rhenium tricarbonyl complexes is highly sensitive to environmental factors. For example, previous studies have shown how intracellular localization of rhenium tricarbonyl complexes as determined by inductively coupled plasma mass spectrometry (ICP-MS) and optical emission spectroscopy (ICP-OES) does not match that obtained via fluorescence microscopy.[43,46,67,96] For these TRIP complexes, we have recently confirmed their cytosolic localization using XRF, demonstrating that in this case fluorescence microscopy works well for predicting their distribution in cells.[70] Furthermore, these XRF studies were used to verify that the axial ligands remain bound to the Re center within cells, showing the remarkable stabilities of these complexes.

ER Stress-Inducing and UPR-Activation Properties. As previously shown,[69] the parent complex in this series, **TRIP-1a**, increases the level of misfolded proteins in cells, which triggers ER stress. Subsequently, activation of the UPR and apoptosis ultimately lead to cell death. On the basis of these results, we aimed to determine if the other TRIP complexes in this library act via a similar mechanism of action. Because we have previously explored the cytotoxic mechanism of **TRIP-1a**

https://dx.doi.org/10.1021/acs.inorgchem.0c01442
Inorg. Chem. 2020, 59, 10285−10303

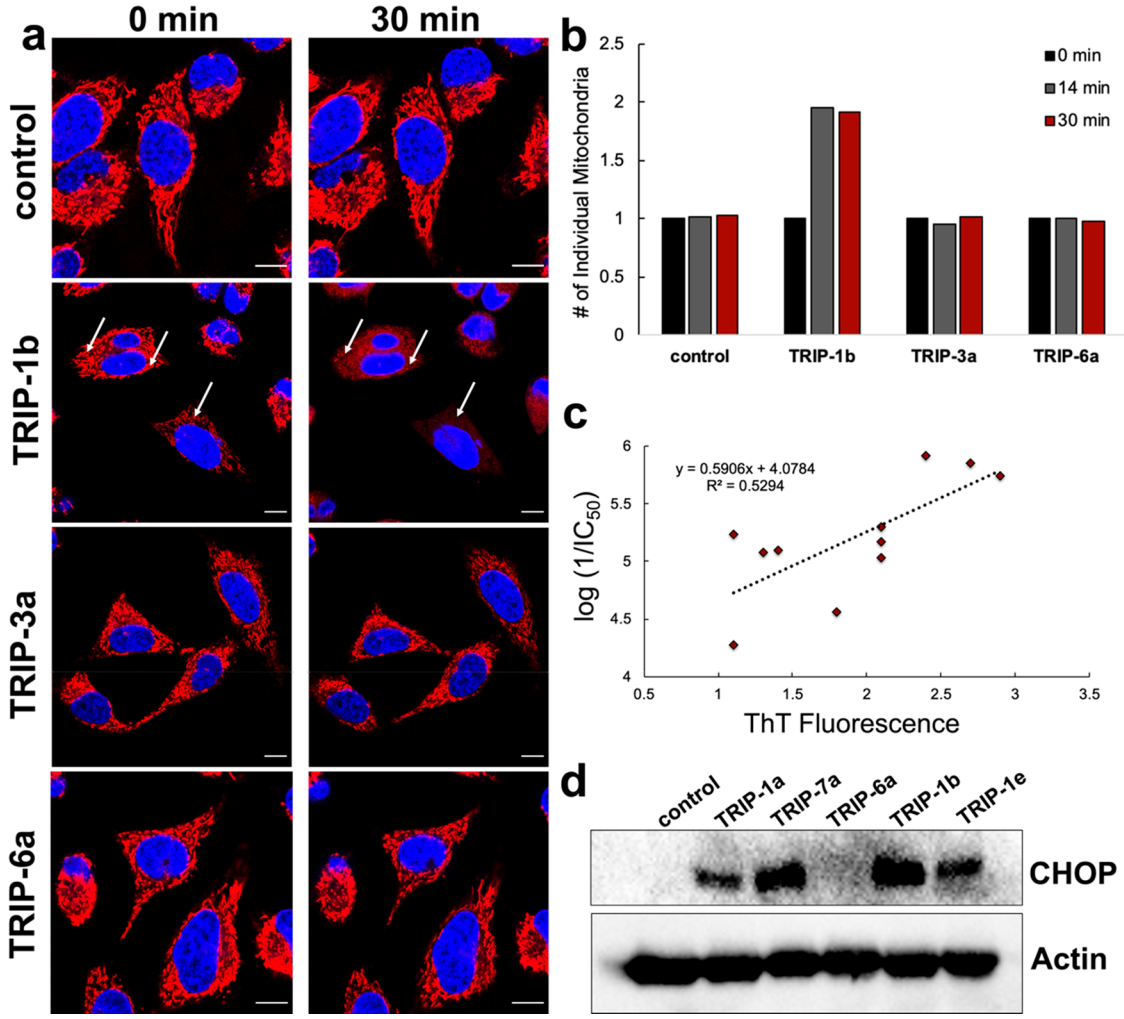

Figure 3. (a) HeLa cells stained with MitoTracker Red (red channel) and Hoechst (blue channel) before (0 min) and after (30 min) exposure to 10 μM of a TRIP complex. For further characterization of this process, Videos 1−4 are included in the Supporting Information. (b) Quantification of the number of individual mitochondria after treatment with 10 μM of a TRIP complex at 0, 14, and 30 min using ImageJ. (c) Correlation of ThT fluorescence in HeLa cells upon treatment with the TRIP derivatives vs the anticancer activity. (d) CHOP Western blot of selected TRIP derivatives after 24-h treatment in HeLa cells.

in great detail, we performed a select subset of assays to investigate whether other TRIP derivatives induce cell death via a similar pathway. Two of the key early phenotypic responses of cells treated with **TRIP-1a** are mitochondrial fission and accumulation of misfolded proteins, processes that happen within the first 30 min of exposure. To determine the importance of mitochondrial fission for the other TRIP complexes, we tested the most and least toxic complexes within this library. Prior to confocal fluorescence microscopy and exposure to 10 μM of a TRIP derivative, HeLa cells were treated with the mitochondria-specific dye, MitoTracker Red, to image the morphology of this organelle, and the nuclear stain Hoechst to identify viable cells. **TRIP-1b**, one of the most cytotoxic complexes in the series, induced rapid rounding of the mitochondria and loss of intensity of the MitoTracker Red dye within several minutes, features that are consistent with mitochondrial fission. Conversely, the least active compounds, **TRIP-3a** and **TRIP-6a**, did not give rise to any changes in mitochondrial morphology over the same time period with an equivalent dose (Figure 3a and Videos 1−4). To more quantitatively analyze these morphological changes, we used an established procedure for counting the number of individual mitochondria with ImageJ.[97] After mitochondrial fission, the number of distinct mitochondria within the cells will increase. The number of mitochondria were quantified at 0, 14, and 30 min in the complex-treated and untreated cells. As shown in Figure 3b, of these three complexes only **TRIP-1b**, the most cytotoxic compound, was able to cause an increase (2-fold) in the number of mitochondria after a 14 min treatment period. These results illustrate that the cytotoxicities of these compounds are related to their ability to cause mitochondrial fission. Furthermore, the phenotypic similarity between the parent complex **TRIP-1a** and the new analogue **TRIP-6a** show that structural modifications to these compounds do not change their mechanisms of action.

To determine if these compounds can cause the accumulation of misfolded or aggregated proteins like **TRIP-1a**, we employed Thioflavin T (ThT), a compound that undergoes an increase in fluorescence upon binding to protein aggregates.[98] This dye is commonly used to detect amyloid β plaques in post-mortem brains of Alzheimer's disease patients.[99,100] HeLa cells were treated with ThT for 2 h prior to being exposed to 10 μM of each of the 11 TRIP derivatives. Changes in fluorescence intensity was monitored at

https://dx.doi.org/10.1021/acs.inorgchem.0c01442
Inorg. Chem. 2020, 59, 10285−10303

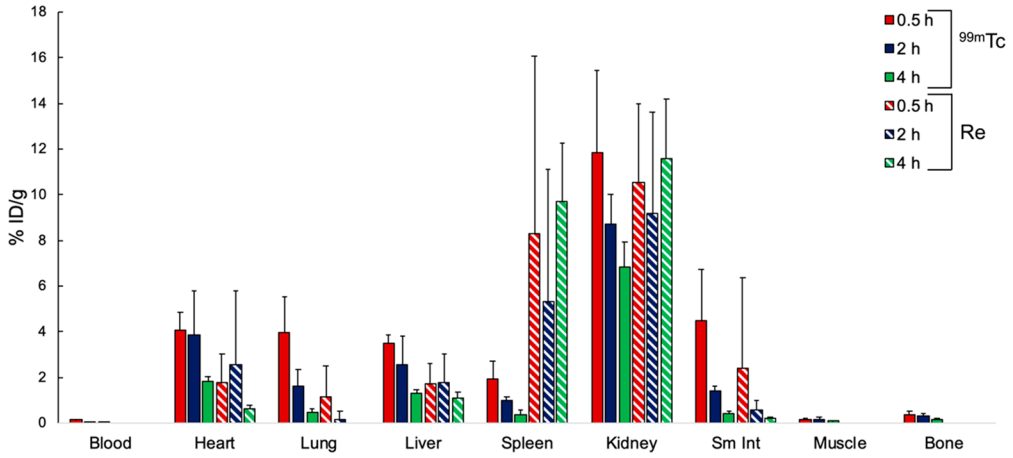

Figure 4. Biodistribution in BALC/c mice of **TRIP-1a** (striped) and **TTIP** (solid). The rhenium content for the blood, muscle, and bone were below detectable levels by ICP-OES.

0 and 30 min post-treatment (Figure S91) using confocal fluorescence microscopy. The results show that the 3 most cytotoxic species, **TRIP-1a**, **TRIP-7a**, and **TRIP-1b**, give rise to a 2-fold or greater increase in ThT fluorescence, demonstrating that these compounds cause protein aggregation. For comparison, the least active compound, **TRIP-6a**, was unable to change the ThT fluorescence levels relative to untreated cells. In analyzing all 11 compounds, a positive linear correlation between the cytotoxicity and the enhancement of ThT fluorescence intensity is apparent (R^2 = 0.53, Figure 3c). The correlation is not as strong as one might expect, which may be due to the assay's limited sensitivity and relatively high deviation. For example, the maximum fluorescence signal increase that we have observed is approximately 3-fold, but the cytotoxicities of the compounds range over an order of magnitude. However, this relationship suggests that the cytotoxic activity of this class of complexes is related to their ability to cause the formation of intracellular protein aggregates. These data show that almost all these complexes induce protein aggregation within 30 min. Thus, this phenotypic response appears to be a general feature of this class of compounds.

As observed previously for **TRIP-1a**, the accumulation of misfolded or aggregated proteins causes cells to shut down translation and initiate the proapoptotic wing of the ER stress response via activation of the UPR and expression of CHOP.[101−103] For **TRIP-1a**, activation of the PERK arm of the UPR occurs, resulting in phosphorylation of eIF2α. This phosphorylation causes global protein synthesis inhibition, activation of the transcription factor ATF4 and CHOP, and finally apoptosis.[104] Thus, we sought to verify that this process proceeds in the same manner for the newly reported TRIP analogues. Translation inhibition was investigated in HeLa cells with the puromycin incorporation assay. Puromycin is a tyrosine mimic that is incorporated into newly synthesized proteins in place of tyrosine. This unnatural amino acid can be detected via Western blot, and its relative amounts present in cells scale with the rate of protein translation.[105] The HeLa cells were treated with 10 μM of each TRIP complex for 2 h, after which puromycin was added. The most potent compounds, **TRIP-1a** and **TRIP-7a**, cause the most efficient inhibition of protein synthesis, as evidenced by the low levels of puromycin incorporation into the proteome. Conversely, the least active complexes, **TRIP-3a** and **TRIP-6a**, have the greatest amount of puromycin incorporation, with levels comparable to that of the untreated cells (Figure S92), indicating that these compounds are not effective translation inhibitors. Thus, these data show that protein translation inhibition is related to the cytotoxic properties of these compounds. As a final confirmation on the ER stress-inducing properties of this class of compounds, we investigated a small subset of these complexes to probe their ability to induce CHOP expression, which is diagnostic for proapoptotic ER stress. HeLa cells were treated with 10 μM of **TRIP-1a**, **TRIP-6a**, **TRIP-7a**, **TRIP-1b**, or **TRIP-1e** for 24 h, prior to analyzing cell lysates for CHOP expression via Western blotting. We found that all complexes tested, except for the least cytotoxic compound **TRIP-6a**, induce CHOP expression after 24 h. In conjunction with the results discussed above, these data collectively show that the cytotoxic TRIP analogues all cause the same ER stress phenotype in cancer cells. Importantly, the cytotoxicities of these complexes are correlated with their abilities to induce this phenotype, indicating that the ER stress response is a key feature of their mechanisms of action. A more in-depth characterization of the ER stress-inducing properties of **TRIP-1a** have been previously reported.[69]

In Vivo Biodistribution and Anticancer Activity of TRIP-1a. A valuable aspect for the development of rhenium-based anticancer agents is the availability of the imaging radionuclide ^{99m}Tc.[106,107] The chemistries of technetium and rhenium are largely similar, and therefore, direct structural analogues of complexes of these metal ions can be prepared.[108−110] In the context of developing new rhenium-based anticancer agents, the corresponding ^{99m}Tc analogues can be used as diagnostic partners to more easily ascertain pharmacokinetic properties of the parent drug candidate. Isonitrile ligands exhibit high affinity for Tc, and several Tc complexes containing ICN ligands have been reported as novel agents for biological imaging.[111−116] To evaluate the potential use of ^{99m}Tc analogues of these TRIP complexes, we synthesized the ^{99m}Tc analogue of the parent compound, *fac*-$[^{99m}Tc(CO)_3(dmphen)(ptolICN)]^+$, called technetium tricarbonyl isonitrile polypyridyl or **TTIP**, using an established approach from *fac*-$[^{99m}Tc(CO)_3(H_2O)_3]^+$.[117] Briefly, an aqueous solution of the ^{99m}Tc starting material was heated at 60 °C for 1 h in the presence of a large excess of the dmphen ligand in water (pH 7). The *p*tolICN ligand was then added, and the mixture was further heated at 60 °C for 90 min to yield

https://dx.doi.org/10.1021/acs.inorgchem.0c01442
Inorg. Chem. 2020, 59, 10285−10303

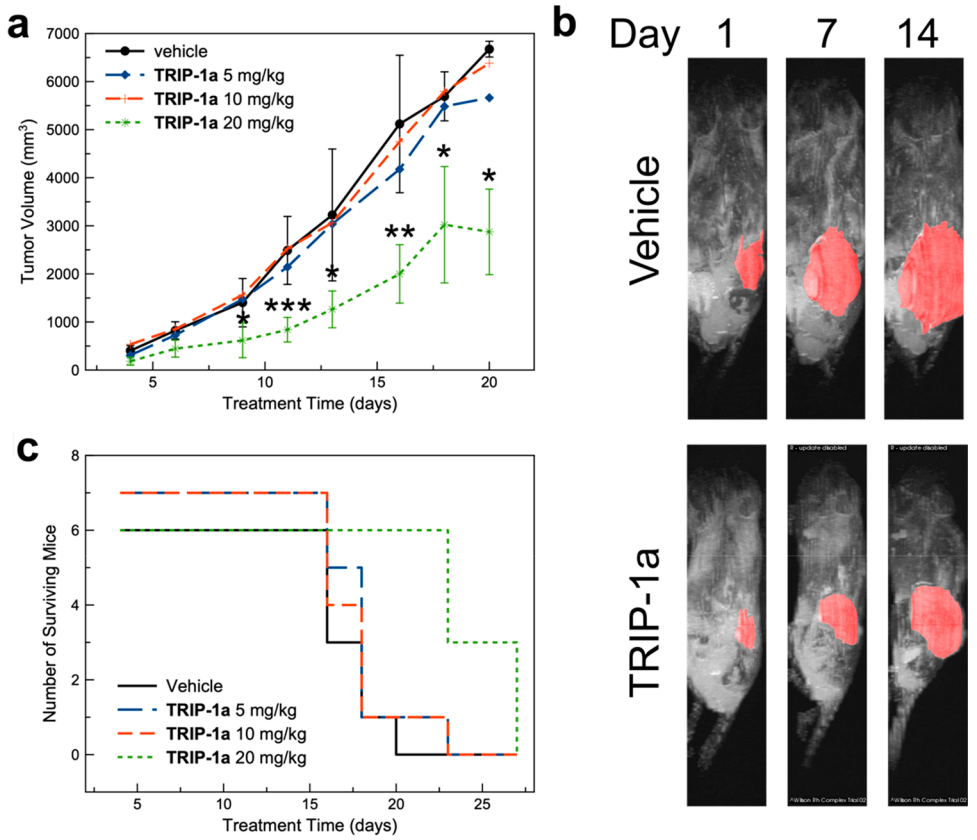

Figure 5. (a) Tumor volume of mice bearing A2780 ovarian cancer xenografts (* = $p < 0.05$, ** = $p < 0.01$, *** = $p < 0.005$). (b) Magnetic resonance images of mice bearing A2780 ovarian cancer xenografts treated with the vehicle control (left) or **TRIP-1a** at 20 mg/kg (right) over the course of 14 days. (c) Kaplan–Meier survival plot of mice treated with **TRIP-1a** throughout the duration of the study.

the product, **TTIP**, which was purified by HPLC. The purity and identity of the product were analyzed via radio-HPLC (Figure S93), which revealed a single peak in the chromatogram with a retention time that matched that of the nonradioactive rhenium analogue **TRIP-1a**.

To evaluate the suitability of **TTIP** as a diagnostic analogue for **TRIP-1a**, we carried out biodistribution studies of these complexes in mice. In general, biodistribution studies of drug candidates are important for determining their in vivo localization and excretion pathways, and they may help identify potential off-target accumulation sites. Furthermore, a comparison of the biodistributions of **TRIP-1a** and **TTIP** is needed to assess their suitability as a matched therapeutic and diagnostic pair. Both of these complexes (~100 μCi ^{99m}Tc and 0.2 μmol Re) were administered simultaneously in BALB/c mice via tail vein injection to determine their biodistribution. Cohorts of mice were sacrificed at 0.5, 2, and 4 h; their organs were excised and then either digested with HNO_3 and analyzed by ICP-OES for Re or subjected to γ counting for quantifying ^{99m}Tc. The results of this biodistribution study are shown in Figure 4. Overall, the distribution of the two complexes is similar, with both exhibiting large kidney and moderate liver uptake. Uptake in these organs suggests that these compounds are undergoing renal and hepatobiliary excretion, similar to other previously reported Re and Tc tricarbonyl complexes.[118] Both **TRIP-1a** and **TTIP** also accumulate in the heart and lungs. The relatively high cardiac uptake may be due to the positive charge of the complexes, which is often observed in ^{99m}Tc complexes, such as the homoleptic isonitrile complex Cardiolite that is used for myocardial perfusion imaging.[119,120] Furthermore, analogous ^{99m}Tc complexes to **TTIP** with the general formula *fac*-$[^{99m}Tc(CO)_3(NN)(ICN)]^+$, where NN are different bpy and phen derivatives and ICN are different isonitriles, exhibit high cardiac uptake, consistent with our observations.[121] The major difference in the distribution of the Re and ^{99m}Tc compounds lies in the spleen. **TRIP-1a** is taken up to a much higher extent in this organ compared to **TTIP**. The spleen is known to be a site of accumulation for macromolecular structures and aggregates.[122−124] Therefore, high Re uptake in this organ may suggest that the compound is forming aggregates in vivo. The much lower concentrations of administered ^{99m}Tc would prevent aggregation of **TTIP**. Collectively, this comparison between the biodistribution of **TRIP-1a** and **TTIP** demonstrates that these compounds exhibit largely similar organ uptake profiles and suggests that ^{99m}Tc analogues of these TRIP complexes are useful partner diagnostic or imaging agents.

On the basis of the promising in vitro anticancer activities of these complexes and favorable biodistribution, we sought to evaluate the in vivo antitumor activity of **TRIP-1a** in mice bearing A2780 ovarian cancer xenografts. We chose to use **TRIP-1a** for these investigations because in addition to its status as the most explored derivative, it also possesses higher solubility than similarly active TRIP complexes such as **TRIP-7a**. Our choice of A2780 ovarian cancer xenografts was motivated by our initial study of **TRIP-1a** that showed this compound to be significantly active against this cell line. Prior to testing the in vivo efficacy of **TRIP-1a**, we performed a maximum tolerated dose (MTD) study, which showed no obvious signs of distress after injection into NSG mice up to

https://dx.doi.org/10.1021/acs.inorgchem.0c01442
Inorg. Chem. 2020, 59, 10285−10303

injections of 40 mg/kg. On the basis of the MTD, mice bearing the A2780 cancer xenografts were treated with 5, 10, or 20 mg/kg of this complex, administered in 20% DMSO/PBS solutions via tail vein injection, twice weekly. Although **TRIP-1a** is soluble up to 2 mM in water or PBS, a DMSO cosolvent was needed to achieve the concentrations necessary for in vivo dosing. Their tumor growth rates and overall health were monitored over 27 days (Figure 5a). For several mice in this study, dosing was discontinued because of weight loss or necrosis at the injection site. The exact dosing schedule and survival time for each mouse in the study is reported in Table S4. The lower doses (5 and 10 mg/kg) of **TRIP-1a** have no effect on tumor growth rate. At 20 mg/kg, however, **TRIP-1a** significantly inhibits tumor growth as shown in Figure 5a,b. From days 10 to 20 after beginning treatment, the 20 mg/kg cohort exhibited tumors with less than half the average volume of the vehicle-treated group. Thus, although **TRIP-1a** was not able to entirely eradicate these tumors, it was able to markedly decrease the tumor growth rate, demonstrating that its anticancer activity is also retained in vivo. These in vivo data can also be analyzed by comparing the survival time of the treated mice relative to the untreated control. Such survival data may be more useful than tumor volumes in comparing the efficacy of drug candidates because different tumor types undergo a wide range of growth rates. The effects of **TRIP-1a** on mouse survival were thus analyzed. In these experiments, mice were sacrificed and did not "survive" if their body weight decreased by 25% or if their tumor burden increased beyond 5500 mm^3. As shown in Figure 5c, 20 mg/kg of **TRIP-1a** prolonged the survival of the tumor-bearing mice by 150% relative to the control group. These results demonstrate that this compound is able to significantly increase mice survival to levels that are comparable to several clinically investigated Ru anticancer agents.[125] Additionally, the mice treated with the highest concentrations of **TRIP-1a** exhibited minimal side effects, as evidenced by minimal body weight changes (Figure S94). Other side effects are discussed in detail in the Supporting Information. These data represent only the fifth example in the literature where the in vivo anticancer activity of a rhenium tricarbonyl complex is demonstrated,[42,67,126−128] and these results support the continued investigation of this interesting class of compounds as antitumor agents.

CONCLUSIONS

The ER has emerged as a promising target for cancer therapy, and a number of recent studies have shown that many metal complexes are effective at triggering ER stress-induced cancer cell death. In this context, the TRIP compounds reported in this study comprise a novel class of metal-based anticancer agents that operate via this mechanism of action. As demonstrated here, the physical and biological properties of these TRIP complexes can be tuned in a modular sense by altering the supporting ligands. From this small library of 11 complexes, our SAR analysis shows that more electron-rich compounds are more cytotoxic. Because a number of spectroscopic features of these complexes are related to their electronic properties, it is possible to identify direct correlations between physical and biological properties. Thus, correlations between spectroscopic methods, such as C≡O and C≡N IR stretching energies and ^{15}N NMR chemical shifts, and cytotoxic activity are apparent. These results highlight the potential predictive power of physical characterization methods for use in biological SARs of novel metal-based anticancer agents.[129−133]

An important assumption that is required for the development of SARs is that all compounds in the library act via a similar mechanism of action. The 11 complexes tested in this study all trigger cell death by inducing ER stress. Furthermore, the ER stress-inducing capacity of the compounds relates to their cytotoxicity, as more cytotoxic complexes elicit greater ER stress responses at equivalent dosing concentrations. These results stand in contrast to a number of other studies on metal anticancer agents, in which subtle ligand modifications led to significant changes in anticancer mechanisms.[35,47,134,135] Although such mechanistic changes are interesting, they present practical challenges in improving and optimizing these types of metal-based drug candidates. Based on the consistent ER stress induction across the TRIP series, modifications of these complexes to optimize important pharmacokinetic properties, such as solubility and clearance rates, can be accomplished without compromising their novel mechanism of anticancer activity.

The promising in vitro anticancer activity and novel mechanism of action of **TRIP-1a** prompted us to further explore its activity in vivo. The use of the ^{99m}Tc analogue, **TTIP**, revealed that the biodistribution of both complexes is comparable, suggesting that these compounds may constitute a theranostic pair. Furthermore, experiments conducted on mice bearing ovarian cancer xenografts indicate that **TRIP-1a** retains anticancer activity in vivo. The activity of this compound, however, is limited in its ability to slow tumor growth but not eradicate the tumor mass in its entirety. Furthermore, difficulties in the formulation and administration of this complex that gave rise to severe local inflammation need to be addressed. As noted above, structural modifications to this class of compounds do not lead to a change in the mechanism of action and can therefore be applied to overcome these issues associated with formulation. Together, the high potency, distinct mechanism of action, broad tunability, and in vivo efficacy of these complexes establish the TRIP scaffold to be a promising class of anticancer agents.

EXPERIMENTAL SECTION

Methods and Materials. Rhenium carbonyl was purchased from Pressure Chemicals (Pittsburgh, PA). $Re(CO)_5Cl$ was synthesized as previously described.[66] The diimine ligands, 2,9-dimethyl-1,10-phenanthroline (dmphen, Cayman Chemical, Ann Arbor, MI), 1,10-phenanthroline (phen, Sigma-Aldrich, St. Louis, MO), 2,2′-bipyridine (bpy, Alfa Aesar, Ward Hill, MA), 4,4′-dimethyl-2,2′-bipyridine (dmbpy, Chem-Impex International Inc., Wood Dale, IL), 4,4′-dimethoxy-2,2′-bipyridine (dmobpy, Sigma-Aldrich, St. Louis, MO), 4,4′-di*tert*-butyl-2,2′-bipyridine (*t*butylbpy, Sigma-Aldrich, St. Louis, MO), and 4,4′-bis(trifluoromethyl)-2,2′-bipyridine (CF_3bpy, Sigma-Aldrich, St. Loius, MO), were used as received. The *fac*-[$Re(CO)_3(NN)Cl$] complexes, where NN is the diimine ligand, were synthesized using previously reported procedures.[136,137] The isonitrile ligands, *para*-tolyl ICN (*p*tolICN), 2,6-dimethylphenyl ICN (2,6-dmphenylICN), 3,5-dimethylphenyl (3,5-dmphenylICN), *para*-methoxyphenyl ICN (*p*-methoxyphenylICN, Sigma-Aldrich, St. Louis, MO), and *para*-chlorophenyl ICN (*p*-chlorophenylICN), were purchased or synthesized from their respective aniline species using a previously reported procedure.[138] *fac*-[$Re(CO)_3$(dmphen)-(*p*tolICN)]OTf (**TRIP-1a**) was synthesized as previously reported.[69] All solvents were ACS grade or higher.

Physical Measurements. NMR samples were prepared as solutions using $CDCl_3$, methanol-d_4, DMSO-d_6, or acetone-d_6 as the solvent. ^1H NMR spectra were acquired on a Bruker 500 MHz

https://dx.doi.org/10.1021/acs.inorgchem.0c01442
Inorg. Chem. 2020, 59, 10285−10303

spectrometer and ^{15}N HMBC spectra were acquired on a Varian Inova 600 MHz spectrometer. ^{1}H NMR chemical shifts were referenced to TMS at 0 ppm and ^{15}N HMBC NMR chemical shifts were referenced to acetonitrile as internal standard (240 ppm vs liquid NH_3 at 0 ppm). Samples for IR spectroscopy were prepared as KBr pellets and were analyzed on a Nicolet Avatar 370 DTGS (ThermoFisher Scientific, Waltham, MA). Analytical chromatography was carried out on a LC-20AT pump with a SPD-20AV UV−vis detector monitored at 270 and 220 nm (Shimadzu, Japan) using an Ultra Aqueous C18 column (100 Å, 5 μm, 250 mm × 4.6 mm, Restek, Bellefonte, PA) at a flow rate of 1 mL/min with a mobile phase containing 0.1% trifluoroacetic acid (TFA) in H_2O or MeOH. The method consisted of 5 min at 10% MeOH, followed by a linear gradient to 100% MeOH over 20 min. High-resolution mass spectra (HRMS) were recorded on an Exactive Orbitrap mass spectrometer in positive ESI mode (ThermoFisher Scientific, Waltham, MA) with samples injected as acetonitrile/water solutions with 1% formic acid. Elemental analyses (C, H, and N) were performed by Atlantic Microlab Inc. (Norcross, GA). UV−visible spectra were recorded on a Cary 8454 UV−vis (Agilent Technologies, Santa Clara, CA) or a Beckman Coulter DU800 UV−vis using 1 cm quartz cuvettes. Fluorescence spectra and photoluminescent quantum yield measurements were carried out on a Beckman Coulter DU800 UV−vis and Varian Eclipse Fluorometer. Electrochemical measurements were carried out using a Pine WaveNow potentiostat with a three-electrode setup consisting of a glassy carbon working electrode, a platinum counter electrode, and a Ag wire quasi-reference electrode. Complexes were dissolved in anhydrous acetonitrile with 0.10 M $[Bu_4N][PF_6]$ (TBAP) as the supporting electrolyte. Potentials were referenced using an internal standard of the ferrocene/ferricenium couple at 0.45 V vs the saturated calomel electrode (SCE).

*Synthesis of fac-[Re(CO)$_3$(phen)(ptolICN)]OTf (**TRIP-2a**).* *fac*-[Re(CO)$_3$(phen)Cl] (0.200 g, 0.41 mmol) was dissolved in dry THF (40 mL), and AgOTf (0.106 g, 0.41 mmol) was added. The mixture was heated at reflux for 3 h, after which the resulting yellow suspension was filtered. To the filtrate, *p*tolICN (0.2 g, 1.7 mmol) was added, and the mixture was heated at reflux overnight. The resulting yellow precipitate was filtered and washed with ∼25 mL of diethyl ether to yield a yellow solid. Yield: 0.126 g (43%). ^{1}H NMR (500 MHz, DMSO-d_6): δ 9.55 (d, J = 5.2 Hz, 2H), 9.07 (d, J = 8.3 Hz, 2H), 8.39 (s, 2 H), 8.19 (dd, J = 8.3, 5.2 Hz, 2H), 7.23−7.18 (m, 4H), 2.26 (s, 3H). IR (KBr, cm^{-1}): 2155 m (C≡N), 2036 s (C≡O), 1973 s (C≡O), 1966 s (C≡O). HR-ESI-MS (positive ion mode): m/z 568.0646 ([M]$^+$, calcd 568.0671). Anal. Calcd for [Re(CO)$_3$(phen)(*p*tolICN)]OTf ($ReC_{24}H_{15}F_3N_3O_6S$): C, 40.22; H, 2.11; N, 5.86. Found: C, 40.15; H, 2.06; N, 5.37.

*Synthesis of fac-[Re(CO)$_3$(bpy)(ptolICN)]OTf (**TRIP-3a**).* *fac*-[Re(CO)$_3$(bpy)Cl] (0.100 g, 0.22 mmol) was dissolved in dry THF (20 mL) and AgOTf (0.056 g, 0.22 mmol) was added. The mixture was heated at reflux for 3 h, after which the resulting yellow suspension was filtered. To the filtrate, *p*tolICN (0.1 g, 0.85 mmol) was added, and the mixture was heated at reflux overnight. The resulting orange solution was evaporated to dryness under vacuum. To the crude solid, 2 mL of toluene was added and the undissolved solid was filtered and washed with ∼15 mL of diethyl ether to yield a pale-yellow solid. Yield: 0.069 g (45%). ^{1}H NMR (500 MHz, $CDCl_3$): δ 9.03 (d, J = 8.2 Hz, 2H), 8.97 (d, J = 5.4 Hz, 2H), 8.38 (t, J = 7.9 Hz, 2H), 7.69 (t, J = 6.5 Hz, 2H), 7.18−7.14 (m, 4H), 2.34 (s, 3H). IR (KBr, cm^{-1}): 2175 m (C≡N), 2038 s (C≡O), 1971 s (C≡O), 1930 s (C≡O). HR-ESI-MS (positive ion mode): m/z 544.0636 ([M]$^+$, calcd 544.0671). Anal. Calcd for [Re(CO)$_3$(bpy)(*p*tolICN)]OTf ($ReC_{22}H_{15}F_3N_3O_6S$): C, 38.15; H, 2.18; N, 6.07. Found: C, 38.41; H, 2.19; N, 6.09.

*Synthesis of fac-[Re(CO)$_3$(dmbpy)(ptolICN)]OTf (**TRIP-4a**).* *fac*-[Re(CO)$_3$(dmobpy)Cl] (0.130 g, 0.27 mmol) was dissolved in dry THF (25 mL), and AgOTf (0.068 g, 0.27 mmol) was added. The mixture was heated at reflux for 3 h, after which the resulting yellow suspension was filtered. To the filtrate, *p*tolICN (0.1 g, 0.85 mmol) was added, and the mixture was heated at reflux overnight. The resulting orange solution was evaporated. The crude residue was then purified using silica gel column chromatography (98% DCM: 2% MeOH). Fractions containing the desired product were pooled, and the solvent was removed under reduced pressure. The product was isolated as a pale yellow solid. Yield: 0.080 g (41%). ^{1}H NMR (500 MHz, $CDCl_3$): δ 8.91 (s, 2H), 8.73 (d, J = 5.7 Hz, 2H), 7.40 (d, J = 5.6 Hz, 2H), 7.18−7.14 (m, 4H), 2.71 (s, 6H), 2.34 (s, 3H). IR (KBr, cm^{-1}): 2176 m (C≡N), 2037 s (C≡O), 1958 s (C≡O), 1934 s (C≡O). HR-ESI-MS (positive ion mode): m/z 572.0941 ([M]$^+$, calcd 572.0984). Anal. Calcd for [Re(CO)$_3$(dmbpy)(*p*tolICN)]OTf ($ReC_{24}H_{19}F_3N_3O_6S$): C, 40.00; H, 2.66; N, 5.83. Found: C, 40.42; H, 2.75; N, 5.83.

*Synthesis of fac-[Re(CO)$_3$(dmobpy)(ptolICN)]OTf (**TRIP-5a**).* *fac*-[Re(CO)$_3$(dmobpy)Cl] (0.100 g, 0.19 mmol) was dissolved in dry THF (20 mL), and AgOTf (0.049 g, 0.19 mmol) was added. The mixture was heated at reflux for 3 h, after which the resulting yellow suspension was filtered. To the filtrate, *p*tolICN (0.1 g, 0.85 mmol) was added, and the mixture was heated at reflux overnight. The solvent was then removed under reduced pressure. To the crude solid, 2 mL of toluene was added, and the undissolved solid was filtered and washed with ∼15 mL of diethyl ether to yield a pale yellow solid. Yield: 0.115 g (81%). ^{1}H NMR (500 MHz, $CDCl_3$): δ 8.62 (d, J = 6.4 Hz, 2 H), 8.48 (d, J = 2.5 Hz, 2 H), 7.19−7.15 (m, 4 H), 7.07−7.05 (m, 2 H), 4.27 (s, 6 H), 2.35 (s, 3 H). IR (KBr, cm^{-1}): 2179 m (C≡N), 2034 s (C≡O), 1957 s (C≡O), 1924 s (C≡O). HR-ESI-MS (positive ion mode): m/z 604.0842 ([M]$^+$, calcd 604.0882). Anal. Calcd for [Re(CO)$_3$(dmobpy)(*p*tolICN)]OTf ($ReC_{24}H_{19}F_3N_3O_8S$): C, 38.30; H, 2.54; N, 5.58. Found: C, 38.54; H, 2.60; N, 5.72.

*Synthesis of fac-[Re(CO)$_3$(CF$_3$bpy)(ptolICN)]OTf (**TRIP-6a**).* *fac*-[Re(CO)$_3$(CF$_3$bpy)Cl] (0.072 g, 0.117 mmol) was dissolved in dry THF (8 mL) and AgOTf (0.032 g, 0.41 mmol) was added. The mixture was heated at reflux for 3 h, after which the resulting yellow suspension was filtered. To the filtrate, *p*tolICN (0.100 g, 0.085 mmol) was added, and the mixture was heated at reflux overnight. The resulting solution was evaporated under reduced pressure. The crude product was dissolved in a minimum amount of DCM (∼5 mL), and this concentrated solution was added to di-isopropyl ether (>100 mL) with rapid stirring. The product that precipitated out was collected by filtration. This process was repeated two more times to obtain an analytically pure compound. Yield: 0.030 g (31%). ^{1}H NMR (500 MHz, acetone-d_6): δ 9.67 (d, J = 5.3 Hz, 2 H), 9.44 (s, 2 H), 8.31 (d, J = 6.0 Hz, 2 H), 7.29−7.25 (m, 4 H), 2.33 (s, 3 H). IR (KBr, cm^{-1}): 2180 m (C≡N), 2045 s (C≡O), 1976 s (C≡O), 1944 s (C≡O). HR-ESI-MS (positive ion mode): m/z 680.0413 ([M]$^+$, calcd 680.0419). Anal. Calcd for [Re(CO)$_3$(CF$_3$bpy)(*p*tolICN)]OTf ($ReC_{24}H_{13}F_9N_3O_6S$): C, 34.79; H, 1.58; N, 5.07. Found: C, 35.04; H, 1.48; N, 4.96.

*Synthesis of fac-[Re(CO)$_3$(tbutylbpy)(ptolICN)]OTf (**TRIP-7a**).* *fac*-[Re(CO)$_3$(*t*butylbpy)Cl] (0.132 g, 0.23 mmol) was dissolved in dry THF (12 mL) and AgOTf (0.060 g, 0.23 mmol) was added. The mixture was heated at reflux for 3 h, after which the resulting yellow suspension was filtered. To the filtrate, *p*tolICN (0.130 g, 1.1 mmol) was added, and the mixture was heated at reflux overnight. The resulting solution was evaporated under reduced pressure, and the crude product was recrystallized from DCM and ether. The material could not be purified sufficiently by recrystallization because of its high solubility. The crude material was purified by preparatory HPLC (50 to 100% MeOH in H_2O containing 0.1% TFA over 30 min) to yield a yellow powder. Elemental analysis data indicates that this complex was isolated with a mixture of TFA (25%) and OTf (75%) counterions (see below). Yield: 0.023 g (12%). ^{1}H NMR (500 MHz, MeOH-d_4): δ 9.04 (d, J = 6.0 Hz, 2 H), 8.71 (s, 2 H), 7.82 (d, J = 6.0 Hz, 2 H), 7.22 (m, 4 H), 2.34 (s, 3 H), 1.51 (s, 18 H). IR (KBr, cm^{-1}): 2175 m (C≡N), 2028 s (C≡O), 1959 s (C≡O), 1931 s (C≡O). HR-ESI-MS (positive ion mode): m/z 656.1882 ([M]$^+$, calcd 656.1923). Anal. Calcd for [Re(CO)$_3$(*t*butylbpy)(*p*tolICN)]-(OTf)$_{0.75}$(TFA)$_{0.25}$ ($ReC_{30.25}H_{31}F_3N_3O_{5.75}S_{0.75}$): C, 45.65; H, 3.93; N, 5.28. Found: C, 45.69; H, 4.03; N, 5.31.

*Synthesis of fac-[Re(CO)$_3$(dmphen)(2,6-dmphenylICN)]OTf (**TRIP-1b**).* *fac*-[Re(CO)$_3$(dmphen)Cl] (0.200 g, 0.38 mmol) was dissolved in dry THF (40 mL) and AgOTf (0.100 g, 0.38 mmol) was added. The mixture was heated at reflux for 3 h, after which the

https://dx.doi.org/10.1021/acs.inorgchem.0c01442
Inorg. Chem. 2020, 59, 10285−10303

resulting yellow suspension was filtered. To the filtrate, 2,6-dmphenylICN (0.2 g, 1.5 mmol) was added, and the mixture was heated at reflux overnight. The THF was removed by rotary evaporation, and the crude solid was dissolved in 2 mL of DCM. The DCM solution was then added dropwise to 50 mL of diethyl ether to precipitate out a pale yellow solid, which was then collected via vacuum filtration and washed with ∼20 mL of ether to yield the pure product. Yield: 0.230 g (80%). ^{1}H NMR (500 MHz, $CDCl_3$): δ 8.79 (d, J = 8.3 Hz, 2 H), 8.19 (s, 2 H), 8.07 (d, J = 8.3 Hz, 2 H), 7.15−6.96 (m, 3 H), 3.34 (s, 6 H), 1.76 (s, 6 H). IR (KBr, cm^{-1}): 2171 m (C≡N), 2033 s (C≡O), 1967 s (C≡O), 1929 s (C≡O). HR-ESI-MS (positive ion mode): m/z 610.1136 ([M]$^+$, calcd 610.1140). Anal. Calcd for [Re(CO)$_3$(dmphen)(2,6-dmphenylICN)]Otf (Re-$C_{27}H_{21}F_3N_3O_6S$): C, 42.74; H, 2.79; N, 5.54. Found: C, 42.88; H, 2.65; N, 5.56.

*Synthesis of fac-[Re(CO)$_3$(dmphen)(3,5-dmphenylICN)]OTf (**TRIP-1c**).* *fac*-[Re(CO)$_3$(dmphen)Cl] (0.220 g, 0.41 mmol) was dissolved in dry THF (20 mL) and AgOTf (0.110 g, 0.43 mmol) was added. The mixture was heated at reflux for 3 h, after which the resulting yellow suspension was filtered. To the filtrate, 3,5-dmphenylICN (0.200 g, 1.5 mmol) was added, and the mixture was heated at reflux overnight. The resulting solution was evaporated under reduced pressure. The crude product was dissolved in a minimum amount of THF (∼5 mL), and this concentrated solution was added to diethyl ether (>100 mL) with rapid stirring. The product that precipitated out was collected by filtration. This process was repeated two more times to obtain the analytically pure compound. ^{1}H NMR (500 MHz, $CDCl_3$): δ 8.75 (d, J = 8.3 Hz, 2 H), 8.16 (s, 2 H), 8.04 (d, J = 8.4 Hz, 2 H), 7.00−6.72 (m, 3 H), 3.32 (s, 6 H), 2.22 (s, 6 H). IR (KBr, cm^{-1}): 2186 m (C≡N), 2036 s (C≡O), 1963 sh (C≡O), 1941 s (C≡O). HR-ESI-MS (positive ion mode): m/z 610.1138 ([M]$^+$, calcd 610.1140). Anal. Calcd for [Re(CO)$_3$(dmphen)(3,5-dmphenylICN)]OTf·0.5$CH_3CH_2OCH_2CH_3$ ($ReC_{29}H_{26}F_3N_3O_{6.5}S$): C, 43.77; H, 3.29; N, 5.28. Found: C, 43.84; H, 2.90; N, 5.79.

*Synthesis of fac-[Re(CO)$_3$(dmphen)(p-methoxyphenylICN)]OTf (**TRIP-1d**).* *fac*-[Re(CO)$_3$(dmphen)Cl] (0.200 g, 0.41 mmol) was dissolved in dry THF, and AgOTf (0.110 g, 0.43 mmol) was added. The mixture was heated at reflux for 3 h, after which the resulting yellow suspension was filtered. To the filtrate, *p*-methoxyphenylICN (0.240 g, 1.8 mmol) was added, and the mixture was heated at reflux overnight. The resulting solution was evaporated under reduced pressure. The crude product was dissolved in a minimum amount of THF (∼5 mL), and this concentrated solution was added to diethyl ether (>100 mL) with rapid stirring. The product that precipitated out was collected by filtration and dissolved in methanol (20 mL). The resulting solution was reduced to <1 mL, and water (10 mL) was added. The mixture was lyophilized to yield a yellow powder. Yield: 0.170 g (77%). ^{1}H NMR (500 MHz, $CDCl_3$): δ 8.63 (d, J = 8.4 Hz, 2 H), 8.07 (s, 2 H), 7.95 (d, J = 8.4 Hz, 2 H), 6.98−6.74 (m, 4 H), 3.72 (s, 3 H), 3.29 (s, 3 H). IR (KBr, cm^{-1}): 2179 m (C≡N), 2036 s (C≡O), 1960 s (C≡O), 1929 s (C≡O). HR-ESI-MS (positive ion mode): m/z 612.0928 ([M]$^+$, calcd 612.0933). Anal. Calcd for [Re(CO)$_3$(dmphen)(*p*-methoxyphenylICN)]Otf (Re-$C_{26}H_{19}F_3N_3O_7S$): C, 41.05; H, 2.52; N, 5.52. Found: C, 41.15; H, 2.60; N, 5.37.

*Synthesis of fac-[Re(CO)$_3$(dmphen)(p-chlorophenylICN)]OTf (**TRIP-1e**).* *fac*-[Re(CO)$_3$(dmphen)Cl] (0.160 g, 0.31 mmol) was dissolved in dry THF and AgOTf (0.080 g, 0.34 mmol) was added. The mixture was heated at reflux for 3 h, after which the resulting yellow suspension was filtered. To the filtrate, *p*-chlorophenylICN (0.160 g, 1.16 mmol) was added, and the mixture was heated at reflux overnight. The resulting solution was evaporated under reduced pressure. The crude product was dissolved in a minimum amount of THF (∼5 mL), and this concentrated solution was added to diethyl ether (>100 mL) with rapid stirring. The product that precipitated out was collected by filtration. This process was repeated two more times to obtain analytically pure compound. Yield: 0.110 g (42%). ^{1}H NMR (500 MHz, $CDCl_3$): δ 8.68 (d, J = 8.4 Hz, 2 H), 8.11 (s, 2 H), 8.01 (d, J = 8.3 Hz, 2 H), 7.30 (d, J = 8.7 Hz, 2 H), 7.15 (d, J = 8.8 Hz, 2 H), 3.32 (s, 6 H). IR (KBr, cm^{-1}): 2185 m (C≡N), 2034 s (C≡O), 1957 s (C≡O), 926 s (C≡O). HR-ESI-MS (positive ion mode): m/z 616.0425 ([M]$^+$, calcd 616.0438). Anal. Calcd for [Re(CO)$_3$(dmphen)(*p*-chlorophenyl-ICN)]OTf·0.25CH_3CN (Re-$C_{25.5}H_{16.75}ClF_3N_{3.25}O_6S$): C, 39.50; H, 2.13; N, 5.87. Found: C, 39.90; H, 2.09; N, 5.79.

X-ray Crystallography. Low-temperature (100 K) X-ray diffraction data was collected on a Rigaku XtaLab Synergy diffractometer equipped with a 4-circle Kappa goniometer and HyPix 6000HE Hybrid Photon Counting (HPC) detector with monochromated Mo Kα radiation (λ = 0.71073 Å). Diffraction images were processed using CrysAlisPro software.[139] The structure was solved through intrinsic phasing using SHELXT[140] and refined against F^2 on all data by full-matrix least-squares with SHELXL[141] following established strategies.[142] All non-hydrogen atoms were refined anisotropically. Hydrogen atoms were included in the model at geometrically calculated positions and refined using a riding model while allowing the torsion angle to refine using the appropriate HFIX command. The isotropic displacement parameters of these hydrogen atoms were set to 1.2 times the U_{eq} of the oxygen atom that they are linked to (1.5 for methyl groups). Details of the structure refinement and selected interatomic distances and angles are listed in Tables S1 and S2.

Emission Quantum Yield. The luminescence quantum yields were measured relative to the standard quinine sulfate (Φ = 0.52, 0.5 M H_2SO_4), which was cross-referenced in our lab to harmaline (Φ = 0.32, 0.05 M H_2SO_4).[143] An excitation wavelength of 350 nm was used for the samples and standards. The compounds were measured as a solution in pH 7.4 PBS containing ≤1% DMSO with the absorbance maintained below 0.1 to prevent inner filter effects.[143] At least five different concentrations of the samples and standards were measured by UV−vis and fluorescence spectroscopy, and the absorbance at 350 nm was plotted versus the integrated emission intensity. The slopes of the resulting lines were used in eq 1:

$$\Phi_{sample} = \Phi_{ref}\frac{S_{sample}\eta^2_{sample}}{S_{ref}\eta^2_{ref}} \quad (1)$$

where Φ_{ref} is the quantum yield of the reference, quinine sulfate; S is the slope of either the sample or the reference, and η is the refractive index.

Lifetime Measurements. Laser excitation for the phosphorescence lifetime measurements was provided by pulsing the 405 nm laser line from a four-line iChrome MLE laser (Toptica Photonics AG, Munich, Germany). The diode laser in the iChrome was triggered by a DG535 Digital Delay/Pulse Generator (Stanford Research, Sunnyvale, CA) at 100 kHz and delivered 100 ns fwhm 405 nm excitation pulses. The 405 nm pulses were fiber-delivered to a sample-filled cuvette, and phosphorescence was collected at 90° through a second fiber for delivery to a Bialkali photomultiplier tube (HC125, Hamamatsu, Bridgewater, NJ) through a 470 nm long pass filter (HQ470lp, Chroma Technology, Bellows Falls, VT). The time-resolved photon counts were collected in 40 ns time bins using a SR430 Multichannel scaler (Stanford Research, Sunnyvale, CA). Data was transferred to a PC via the SR430 GPIB bus and fit to the standard exponential decay model. Measurements were collected in PBS solutions at 10 μM. For deoxygenated measurements, nitrogen gas was bubbled into the PBS solutions for 20 min, and then the lifetime was determined.

Cell Culture and Cytotoxicity. The HeLa (cervical cancer) cell line were obtained from American Type Culture Collection (ATCC) and cultured using Dulbecco's Modified Eagle's Medium (DMEM) supplemented with 10% fetal bovine serum (FBS). HeLa cells were grown in a humidified incubator at 37 °C with an atmosphere of 5% CO_2. Cells were passed at 80−90% confluence using trypsin/EDTA. Cells were tested monthly for mycoplasma contamination with the PlasmoTest mycoplasma detection kit from InvivoGen.

The compounds **TRIP-1a**, **TRIP-3a**, **TRIP-4a**, and **TRIP-5a** were dissolved in PBS (pH 7.4) to prepare 0.5−1 mM stock solutions. The compounds **TRIP-6a**, **TRIP-7a**, **TRIP-1b**, **TRIP-1c**, **TRIP-1d**, and

https://dx.doi.org/10.1021/acs.inorgchem.0c01442
Inorg. Chem. 2020, 59, 10285−10303

TRIP-1e were dissolved in DMSO to prepare 5−20 mM stock solutions. **TRIP-2a** stock solutions were prepared in both PBS (pH 7.4) and DMSO, and the IC_{50} values were the same for both types of stock solutions, indicating that the stability of these complexes is the same in these solutions. For cell viability studies, all cells were grown to 80−90% confluence, detached with trypsin/EDTA, seeded in 96-well plates at 4000 cells/well in 100 μL of growth media, and incubated for 24 h. The medium was removed and replaced with fresh medium (200 μL) containing varying dilutions of either the rhenium compounds or media. The cells were then incubated for 48 h. The additional 48 h incubation was performed to ensure that the cells were in the logarithmic growth phase and that the cells had adequate time to regrow after exposure to the complexes. The medium was removed from the wells, and 3-(4,5-dimethylthiazol-2-yl)-2,5-tetrazolium bromide (MTT) in DMEM (200 μL, 1 mg/mL) was added. After 4 h, the MTT/DMEM solution was removed, and the formazan crystals were dissolved in 200 μL of an 8:1 mixture of DMSO and pH 10 glycine buffer. The absorbance at 570 nm in each well was measured using a BioTek Synergy HT plate reader. Cell viability was determined by normalizing the absorbance of the treated wells to untreated wells. The % viability data shown is an average of three independent experiments with six replicates per concentration.

Confocal Fluorescence Microscopy. A total of 1×10^5 HeLa cells were seeded onto 35 mm glass bottom dishes. After 24 h, the cells were treated with the rhenium compound (10 μM) in DMEM media. After 2 h, the media was removed, the cells were washed with PBS, and fresh media was added. Right before imaging, the media was removed and imaging buffer was added (20 mM HEPES pH 7.4, 135 mM NaCl, 5 mM KCl, 1.8 mM $CaCl_2$, 1 mM $MgCl_2$, 1 mg/mL glucose, and 1 mg/mL bovine serum albumin). The cells were imaged with a Zeiss LSM 800 or Zeiss LSM 880 confocal laser-scanning microscope. The rhenium complexes were imaged using a 405 nm laser excitation with a 410−550 nm emission filter, and images were processed using ImageJ software. The cellular images were analyzed using ImageJ software, and the corrected total cell fluorescence (CTCF) was determined using eq 2:

$$\text{CTCF} = \text{integrated density} - (\text{area of cell} \times \text{mean fluorescence of background reading}) \quad (2)$$

The average of at least 10 cells was used to determine the average CTCF.

Mitochondria Morphology Experiment by Fluorescence Microscopy. For time-lapse experiments, HeLa cells were incubated with MitoTracker Red FM (1 μL of 1 mM dye) and Hoechst 33342 (1 μL of 20 mM dye) for 30 min, separately. After incubation with the dyes, the media was removed, the cells were washed with PBS, and fresh media was added. At the microscope, the rhenium compounds were diluted in imaging buffer to reach a final concentration of 10 μM and the cells were imaged over 2 min increments for a maximum of 30 min. MitoTracker Red FM was excited with a 561 nm laser with an emission filter from 630−700 nm. Hoechst 33342 was excited with a 405 nm laser with an emission filter of 410−550 nm. The cellular images were analyzed using ImageJ software, and the mitochondrial morphology was analyzed using a previously reported procedure.[97]

Thioflavin T (ThT) Assay by Fluorescence Microscopy. A total of approximately 1×10^5 HeLa cells were seeded onto 35 mm glass bottom dishes. After 24 h, the cells were treated with 5 μM ThT for 2 h. After 2 h, the media was removed, cells were washed with 1 mL PBS, and 1 mL of fresh media was added to the dishes. At the microscope, the rhenium complexes (10 μM) were diluted in imaging buffer and imaged at 0 and 30 min. The cells were imaged using a 405 nm laser excitation with a 410−550 nm green emission filter. The cellular images were analyzed using ImageJ software, and the CTCF was calculated using eq 2.

Immunoblotting. HeLa cells were treated with the vehicle control (DMSO) or the TRIP derivative (10 μM) for 24 h. Cells were lysed in TBS buffer (50 mM Tris, pH7.5, 150 mM NaCl, 1 mM EDTA) containing 1% Triton X-100, 2 U/ml DNase and protease inhibitor cocktail tablet (Cell Signaling). The lysates were incubated on ice for 30 min, followed by heating for 10 min in SDS-PAGE sample buffer (50 mM Tris (pH 6.8), 100 mM dithiothreitol, 2% SDS, 0.1% bromophenol blue, 10% glycerol). Proteins were separated on SDS-PAGE and transferred to PVDF membranes (Fisher). Membranes were blocked in TBS containing 5% bovine serum albumin and 0.1% Tween-20 for 1 h, followed by incubation with the primary antibody CHOP (Cell Signaling) overnight at 4 °C. After incubation with the horseradish peroxidase-coupled secondary antibody at room temperature for 1 h, immunoblots were visualized using enhanced chemiluminescence (ECLPlus, GE Healthcare), and β-Actin antibody (Sigma-Aldrich) was used to quantify β-actin as a loading control.

Puromycin Labeling of Proteins. HeLa cells were treated with the vehicle control (DMSO) or the TRIP derivative (10 μM) for 2 h. After 2 h, 10 μM puromycin was added to the medium, and cells were harvested 10 min after the addition of puromycin. Cells were lysed in TBS buffer (50 mM Tris, pH 7.5, 150 mM NaCl, 1 mM EDTA) containing 1% Triton X-100, 2 U/ml DNase and protease inhibitor cocktail tablet (Cell Signaling). The lysates were incubated on ice for 30 min, followed by heating for 10 min in SDS-PAGE sample buffer (50 mM Tris (pH 6.8), 100 mM dithiothreitol, 2% SDS, 0.1% bromophenol blue, 10% glycerol). Proteins were separated on SDS-PAGE and transferred to PVDF membranes (Fisher). Membranes were blocked in TBS containing 5% nonfat milk and 0.1% Tween-20 for 1 h. Puromycin-labeled polypeptides were then quantified by incubating membranes with antipuromycin (Developmental Studies Hybridoma Bank, #PMY-2A4) overnight at 4 °C and then with horseradish peroxidase-coupled secondary antibodies at room temperature for 1 h. Immunoblots were visualized using enhanced chemiluminescence, and β-actin antibody (Sigma-Aldrich) was used to quantify β-actin as a loading control.

Synthesis of TTIP. *General Methods.* RadioHPLC analysis was carried out using a Shimadzu HPLC-20AR instrument equipped with a binary gradient, pump, UV−vis detector, autoinjector, and Laura radiodetector. UV absorption was recorded at 254 and 280 nm; samples were analyzed using a C18 column (Phenomenex Gemini C18, 150 mm × 4.60 mm), 0.8 mL/min flow, with mobile phase. Method 1. Solvent A: 50 mM TEAP (tetraethylammonium phosphate, pH 2) in water; solvent B: MeOH. 0−2 min: 5% B; 2−14 min: 5−95% B; 14−19 min: 95% B; 19−19.5 min: 95−5% B; 19.5−25 min: 5% B.

Purification of 2,9-Dimethyl-1,10-phenantholine (dmphen). 2,9-Dimethyl-1,10-phenantholine (98% purity) as received from Sigma-Aldrich was repurified using automated, reverse phase C18 chromatography. The identity of the product was confirmed with mass spectrometry.

Synthesis of ***TTIP****.* ^{99m}Tc-labeling involved the initial synthesis of technetium tricarbonyl precursor, $[^{99m}Tc(CO)_3(H_2O)_3]^+$. Sodium pertechnetate, $Na[^{99m}TcO_4]$, was eluted from a ^{99}Mo/^{99m}Tc sterile generator as a 1.0 mL saline solution (0.9% v/v) and was provided by Triad Isotopes (Hicksville, NY). The radioactive solution was added to a sealed vial containing boranocarbonate (4 mg), sodium tartrate (7 mg), and sodium borate decahydrate (7 mg). The carbonylation was carried out under heating for 40 min at 100 °C using an oil bath. The solution was cooled to room temperature. A separate solution of ligand (10^{-4} M in MeOH) was prepared. To the aqueous $[^{99m}Tc(CO)_3(H_2O)_3]^+$ solution (34.7 mCi, 1 mL) was added to 1 M HCl (150−180 μL) to adjust the pH to 7. A 500 μL aliquot was removed and mixed with dmphen ligand stock solution (100 μL, 10 mM). The mixture was heated to 60 °C for 30 min under vigorous stirring in a sealed reaction vessel. The reaction was analyzed using analytical radioHPLC. Preparative purification of the complexes was carried out using large-volume HPLC injections followed by manual collection of the assigned product peak. 100 μL of 10 mM dmphen was added, and the solution was heated for 30 min at 60 °C. After confirmation of formation of the $[^{99m}Tc(CO)_3(dmphen)(H_2O)]^+$ intermediate, the isonitrile (100 μL of 10 mM stock solution) was added, and the reaction mixture was heated at 60 °C for 90 min to afford $[^{99m}Tc(CO)_3(dmphen)(ptolICN)]^+$ (**TTIP**) as confirmed by HPLC. Following purification by HPLC, the solvent was removed

https://dx.doi.org/10.1021/acs.inorgchem.0c01442
Inorg. Chem. 2020, 59, 10285−10303

in vacuo and the product (1.525 mCi) was resuspended for injection in 1.35 mL PBS pH 7.4. The purified, final, nondecay-corrected radiochemical yield was 4.3%.

Biodistribution of ***TTIP***. All animal experiments for biodistribution were conducted according to the guidelines of the Institutional Animal Care and Use Committee (IACUC) of Stony Brook University at the Department of Laboratory Animal Resources (DLAR), Stony Brook Medicine. Female BALB/c mice (6 weeks old, Taconic Biosciences, Taconic NY) were intravenously injected with 51−104 μCi of **TTIP** and 0.2 μmol of **TRIP-1a** via a tail vein catheter in 10% EtOH/saline. Mice were sacrificed at 1, 2, and 4 h post injection. The following organs were harvested and collected: blood (obtained via cardiac puncture), heart, liver, lung, kidney, spleen, small intestine, muscle (thigh), bone (femur), and urine. Urine was collected for metabolite analysis via bladder puncture. Radioactivity was counted using a gamma counter. Radioactivity associated with each organ was expressed as % ID/g. Metabolite analysis of blood and urine was carried out by fractioned collection of HPLC eluent and subsequent reconstruction of the chromatogram. For ICP-OES analysis of rhenium content, organs were incubated with nitric acid (3 mL) and the organs were left to digest for 20 h at 25 °C. 300 μL of organ digest was diluted with 3 mL of ICP diluent and subsequently analyzed for Re content using ICP-OES. Tb (20 ppm) was used as an internal standard. Percent injected dose per gram (% ID/g) was calculated based on injection volumes used for each animal (0.2 μmol for mouse 4; producing an administered Re dose was 10 μmol/kg with 0.2 μmol (mouse)).

In Vivo Mouse Studies. *Animals*. All animal procedures for tumor xenograft studies were approved by the Cornell University IACUC No. 2017-0035 and were in accordance with Cornell University policies on the care, welfare, and treatment of laboratory animals. Blinding occurred during body weight and tumor volume analyses. For the in vivo tumor growth studies, NSG mice (Jackson Laboratory 005557) were used at ∼7 weeks old for evaluation in NSG mice bearing A2780 ovarian cancer xenografts. Each cage contained up to 5 mice and offered Teklad irradiated rodent food by Envigo and water. The animal room was set to maintain between 68 and 73 °F and a relative humidity of 40−45%; there were a minimum of 15 room air changes per hour and a 12 h light/dark cycle, which was interrupted for study-related activities. Information on tumor inoculation is described under the In Vivo Tumor Growth Inhibition. Mice were euthanized using carbon dioxide administration. Mice were placed into an empty, clean cage and were administered carbon dioxide at a flow rate of 3.5 L per second; mice were removed from the cage after respirations had ceased for a period of 1 min.

In Vivo Tumor Growth Inhibition. A2780 ovarian cancer xenografts were resected from propagation mice and implanted subcutaneously in the left flank of 35 mice. The animals were then separated into five groups of at least five, and tumors were allowed to grow over 100 mm^3. Mice were then injected twice weekly intravenously with either vehicle (20% DMSO in PBS) or solutions of **TRIP-1a** (5, 10, or 20 mg/kg in 20% DMSO/PBS). Their body weights and tumor volumes were monitored over 27 days. Tumor volumes were estimated by measuring the width (W) and length (L) of the tumor using a caliper and calculated using eq 3, where width was equal to the smaller value of the caliper measurements:

$$\text{volume} = \frac{W^2 L}{2} \tag{3}$$

After treatment completion or upon tumor volumes reaching greater than 30 mm in any one dimension or a total tumor burden of 5500 mm^3, mice were euthanized, and tumors were dissected and weighed. Major organs (kidneys, liver, spleen, heart, lung, brain, and tumor) were harvested and fixed in 10% formalin.

Ex Vivo Tissue Processing for H&E Stained Slide Review. Fixed tissues were trimmed, placed on cassettes, and loaded onto a tissue processor for embedding with paraffin wax. The embedded tissues were then sectioned, mounted onto glass slides, and dried. These slides were then stained with H&E using an automated H&E stainer. Slide review was conducted at the Section of Anatomic Pathology within the Animal Health Diagnostic Center at Cornell University.

■ ASSOCIATED CONTENT

Supporting Information

The Supporting Information is available free of charge at https://pubs.acs.org/doi/10.1021/acs.inorgchem.0c01442.

X-ray crystallographic data parameters and interatomic bond lengths and angles, ^{1}H and ^{15}N HMBC NMR spectra, IR spectra, HPLC chromatograms, cyclic voltammograms, UV−vis and emission spectra, transient emission decay profiles, dose−response curves, confocal fluorescence microscopy images, electronic parameter correlations, Western blots, and mice body weights and dosing times (PDF)

Video 1: **TRIP-1b** (AVI)

Video 2: **TRIP-3a** (AVI)

Video 3: **TRIP-6a** (AVI)

Video 4: control (AVI)

Accession Codes

CCDC 2000501 contains the supplementary crystallographic data for this paper. These data can be obtained free of charge via www.ccdc.cam.ac.uk/data_request/cif, or by emailing data_request@ccdc.cam.ac.uk, or by contacting The Cambridge Crystallographic Data Centre, 12 Union Road, Cambridge CB2 1EZ, UK; fax: +44 1223 336033.

■ AUTHOR INFORMATION

Corresponding Author

Justin J. Wilson − *Department of Chemistry and Chemical Biology, Cornell University, Ithaca, New York 14853, United States*; orcid.org/0000-0002-4086-7982; Email: jjw275@cornell.edu

Authors

Sierra C. Marker − *Department of Chemistry and Chemical Biology, Cornell University, Ithaca, New York 14853, United States*

A. Paden King − *Department of Chemistry and Chemical Biology, Cornell University, Ithaca, New York 14853, United States*

Samantha Granja − *Department of Chemistry and Chemical Biology, Cornell University, Ithaca, New York 14853, United States*

Brett Vaughn − *Department of Chemistry, Stony Brook University, Stony Brook, New York 11794, United States*

Joshua J. Woods − *Department of Chemistry and Chemical Biology and Robert F. Smith School for Chemical and Biomolecular Engineering, Cornell University, Ithaca, New York 14853, United States*; orcid.org/0000-0002-6213-4093

Eszter Boros − *Department of Chemistry, Stony Brook University, Stony Brook, New York 11794, United States*; orcid.org/0000-0002-4186-6586

Complete contact information is available at: https://pubs.acs.org/10.1021/acs.inorgchem.0c01442

Author Contributions

‡S.C.M. and A.P.K. contributed equally.

Notes

The authors declare no competing financial interest.

https://dx.doi.org/10.1021/acs.inorgchem.0c01442
Inorg. Chem. 2020, 59, 10285−10303

■ ACKNOWLEDGMENTS

This research was supported by the College of Arts and Sciences at Cornell University, the Cornell Technology Licensing Office Cornell Technology Acceleration and Maturation (CTAM) fund, and the Office of the Assistant Secretary of Defense for Health Affairs through the Ovarian Cancer Research Program under Award No. W81XWH-17-1-0097. A.P.K. thanks the National Institute of Health, National Institute of General Medical Sciences, for a Chemical Biology Interface (CBI) Training Grant (Grant Number T32GM008500). This work made use of the NMR facility at Cornell University, which is supported, in part, by the NSF under Award Number CHE-1531632. We thank Prof. Warren Zipfel and Prof. Jeremy Baskin for assistance with the fluorescence decay lifetime measurements and allowing us to use their confocal fluorescence microscope for acquiring all the live cell images, respectively.

■ REFERENCES

(1) Wheate, N. J.; Walker, S.; Craig, G. E.; Oun, R. The Status of Platinum Anticancer Drugs in the Clinic and in Clinical Trials. *Dalton Trans.* **2010**, *39*, 8113−8127.
(2) Ohmichi, M.; Hayakawa, J.; Tasaka, K.; Kurachi, H.; Murata, Y. Mechanisms of Platinum Drug Resistance. *Trends Pharmacol. Sci.* **2005**, *26*, 113−116.
(3) Martin, L. P.; Hamilton, T. C.; Schilder, R. J. Platinum Resistance: The Role of DNA Repair Pathways. *Clin. Cancer Res.* **2008**, *14*, 1291−1295.
(4) Miller, R. P.; Tadagavadi, R. K.; Ramesh, G.; Reeves, W. B. Mechanisms of Cisplatin Nephrotoxicity. *Toxins* **2010**, *2*, 2490−2518.
(5) Oun, R.; Moussa, Y. E.; Wheate, N. J. The Side Effects of Platinum-Based Chemotherapy Drugs: A Review for Chemists. *Dalton Trans.* **2018**, *47*, 6645−6653.
(6) Healy, S. J. M.; Gorman, A. M.; Mousavi-Shafaei, P.; Gupta, S.; Samali, A. Targeting the Endoplasmic Reticulum-Stress Response as an Anticancer Strategy. *Eur. J. Pharmacol.* **2009**, *625*, 234−246.
(7) Liu, Y.; Ye, Y. Proteostasis Regulation at the Endoplasmic Reticulum: A New Perturbation Site for Targeted Cancer Therapy. *Cell Res.* **2011**, *21*, 867−883.
(8) Vincenz, L.; Jäger, R.; O'Dwyer, M.; Samali, A. Endoplasmic Reticulum Stress and the Unfolded Protein Response: Targeting the Achilles Heel of Multiple Myeloma. *Mol. Cancer Ther.* **2013**, *12*, 831−843.
(9) Banerjee, S.; Zhang, W. Endoplasmic Reticulum: Target for Next-Generation Cancer Therapy. *ChemBioChem* **2018**, *19*, 2341−2343.
(10) Vandewynckel, Y.-P.; Laukens, D.; Geerts, A.; Bogaerts, E.; Paridaens, A.; Verhelst, X.; Janssens, S.; Heindryckx, F.; Van Vlierberghe, H. The Paradox of the Unfolded Protein Response in Cancer. *Anticancer Res.* **2013**, *33*, 4683−4694.
(11) Yadav, R. K.; Chae, S.-W.; Kim, H.-R.; Chae, H. J. Endoplasmic Reticulum Stress and Cancer. *J. Cancer Prev.* **2014**, *19*, 75−88.
(12) Walczak, A.; Gradzik, K.; Kabzinski, J.; Przybylowska-Sygut, K.; Majsterek, I. The Role of the ER-Induced UPR Pathway and the Efficacy of Its Inhibitors and Inducers in the Inhibition of Tumor Progression. *Oxid. Med. Cell. Longev.* **2019**, 5729710.
(13) Mann, M. J.; Hendershot, L. M. UPR Activation Alters Chemosensitivity of Tumor Cells. *Cancer Biol. Ther.* **2006**, *5*, 736−740.
(14) Riha, R.; Gupta-Saraf, P.; Bhanja, P.; Badkul, S.; Saha, S. Stressed Out - Therapeutic Implications of ER Stress Related Cancer Research. *Oncomedicine* **2017**, *2*, 156−167.
(15) Xu, D.; Liang, S. Q.; Yang, H.; Lüthi, U.; Riether, C.; Berezowska, S.; Marti, T. M.; Hall, S. R. R.; Bruggmann, R.; Kocher, G. J.; Schmid, R. A.; Peng, R. W. Increased Sensitivity to Apoptosis upon Endoplasmic Reticulum Stress-Induced Activation of the Unfolded Protein Response in Chemotherapy-Resistant Malignant Pleural Mesothelioma. *Br. J. Cancer* **2018**, *119*, 65−75.
(16) Lin, Y.; Jiang, M.; Chen, W.; Zhao, T.; Wei, Y. Cancer and ER Stress: Mutual Crosstalk between Autophagy, Oxidative Stress and Inflammatory Response. *Biomed. Pharmacother.* **2019**, *118*, 109249.
(17) Fribley, A.; Zhang, K.; Kaufman, R. J. Regulation of Apoptosis by the Unfolded Protein Response. *Methods Mol. Biol.* **2009**, *559*, 191−204.
(18) Sano, R.; Reed, J. C. ER Stress-Induced Cell Death Mechanisms. *Biochim. Biophys. Acta, Mol. Cell Res.* **2013**, *1833*, 3460−3470.
(19) Cao, S. S.; Kaufman, R. J. Endoplasmic Reticulum Stress and Oxidative Stress in Cell Fate Decision and Human Disease. *Antioxid. Redox Signaling* **2014**, *21*, 396−413.
(20) Rashid, H.-O.; Yadav, R. K.; Kim, H.-R.; Chae, H.-J. ER Stress: Autophagy Induction, Inhibition and Selection. *Autophagy* **2015**, *11*, 1956−1977.
(21) Obeng, E. A.; Carlson, L. M.; Gutman, D. M.; Harrington, W. J.; Lee, K. P.; Boise, L. H. Proteasome Inhibitors Induce a Terminal Unfolded Protein Response in Multiple Myeloma Cells. *Blood* **2006**, *107*, 4907−4916.
(22) Meng, X.; Leyva, M. L.; Jenny, M.; Gross, I.; Benosman, S.; Fricker, B.; Harlepp, S.; Hébraud, P.; Boos, A.; Wlosik, P.; Bischoff, P.; Sirlin, C.; Pfeffer, M.; Loeffler, J.-P.; Gaiddon, C. A Ruthenium-Containing Organometallic Compound Reduces Tumor Growth through Induction of the Endoplasmic Reticulum Stress Gene CHOP. *Cancer Res.* **2009**, *69*, 5458−5466.
(23) Chow, M. J.; Licona, C.; Yuan Qiang Wong, D.; Pastorin, G.; Gaiddon, C.; Ang, W. H. Discovery and Investigation of Anticancer Ruthenium−Arene Schiff-Base Complexes via Water-Promoted Combinatorial Three-Component Assembly. *J. Med. Chem.* **2014**, *57*, 6043−6059.
(24) Chow, M. J.; Babak, M. V.; Wong, D. Y. Q.; Pastorin, G.; Gaiddon, C.; Ang, W. H. Structural Determinants of p53-Independence in Anticancer Ruthenium-Arene Schiff-Base Complexes. *Mol. Pharmaceutics* **2016**, *13*, 2543−2554.
(25) Chow, M. J.; Alfiean, M.; Pastorin, G.; Gaiddon, C.; Ang, W. H. Apoptosis-Independent Organoruthenium Anticancer Complexes That Overcome Multidrug Resistance: Self-Assembly and Phenotypic Screening Strategies. *Chem. Sci.* **2017**, *8*, 3641−3649.
(26) Zhang, J. J.; Sun, R. W. Y.; Che, C. M. A Dual Cytotoxic and Anti-Angiogenic Water-Soluble Gold(III) Complex Induces Endoplasmic Reticulum Damage in HeLa Cells. *Chem. Commun.* **2012**, *48*, 3388−3390.
(27) Sun, R. W. Y.; Lok, C. N.; Fong, T. T. H.; Li, C. K. L.; Yang, Z. F.; Siu, A. F. M.; Che, C. M. A Dinuclear Cyclometalated Gold(III)-Phosphine Complex Targeting Thioredoxin Reductase Inhibits Hepatocellular Carcinoma in vivo. *Chem. Sci.* **2013**, *4*, 1979−1988.
(28) Huang, K.-B.; Wang, F.-Y.; Tang, X.-M.; Feng, H.-W.; Chen, Z.-F.; Liu, Y.-C.; Liu, Y.-N.; Liang, H. Organometallic Gold(III) Complexes Similar to Tetrahydroisoquinoline Induce ER-Stress-Mediated Apoptosis and Pro-Death Autophagy in A549 Cancer Cells. *J. Med. Chem.* **2018**, *61*, 3478−3490.
(29) Cao, R.; Jia, J.; Ma, X.; Zhou, M.; Fei, H. Membrane Localized Iridium(III) Complex Induces Endoplasmic Reticulum Stress and Mitochondria-Mediated Apoptosis in Human Cancer Cells. *J. Med. Chem.* **2013**, *56*, 3636−3644.
(30) Mandal, S.; Poria, D. K.; Ghosh, R.; Ray, P. S.; Gupta, P. Development of a Cyclometalated Iridium Complex with Specific Intramolecular Hydrogen-Bonding That Acts as a Fluorescent Marker for the Endoplasmic Reticulum and Causes Photoinduced Cell Death. *Dalton Trans.* **2014**, *43*, 17463−17474.
(31) Tripathy, S. K.; De, U.; Dehury, N.; Laha, P.; Panda, M. K.; Kim, H. S.; Patra, S. Cyclometallated Iridium Complexes Inducing Paraptotic Cell Death like Natural Products: Synthesis, Structure and Mechanistic Aspects. *Dalton Trans.* **2016**, *45*, 15122−15136.
(32) Yang, C.; Mehmood, F.; Lam, T. L.; Chan, S. L. F.; Wu, Y.; Yeung, C. S.; Guan, X.; Li, K.; Chung, C. Y. S.; Zhou, C. Y.; Zou, T.; Che, C. M. Stable Luminescent Iridium(III) Complexes with Bis(*N*-

https://dx.doi.org/10.1021/acs.inorgchem.0c01442
Inorg. Chem. 2020, 59, 10285−10303

Heterocyclic Carbene) Ligands: Photo-Stability, Excited State Properties, Visible-Light-Driven Radical Cyclization and CO_2 Reduction, and Cellular Imaging. *Chem. Sci.* **2016**, *7*, 3123−3136.
(33) Nam, J. S.; Kang, M.-G.; Kang, J.; Park, S.-Y.; Lee, S. J. C.; Kim, H.-T.; Seo, J. K.; Kwon, O.-H.; Lim, M. H.; Rhee, H.-W.; Kwon, T.-H. Endoplasmic Reticulum-Localized Iridium(III) Complexes as Efficient Photodynamic Therapy Agents via Protein Modifications. *J. Am. Chem. Soc.* **2016**, *138*, 10968−10977.
(34) Yuan, B.; Liu, J.; Guan, R.; Jin, C.; Ji, L.; Chao, H. Endoplasmic Reticulum Targeted Cyclometalated Iridium(III) Complexes as Efficient Photodynamic Therapy Photosensitizers. *Dalton Trans.* **2019**, *48*, 6408−6415.
(35) Suntharalingam, K.; Johnstone, T. C.; Bruno, P. M.; Lin, W.; Hemann, M. T.; Lippard, S. J. Bidentate Ligands on Osmium(VI) Nitrido Complexes Control Intracellular Targeting and Cell Death Pathways. *J. Am. Chem. Soc.* **2013**, *38*, 14060−14063.
(36) Suntharalingam, K.; Lin, W.; Johnstone, T. C.; Bruno, P. M.; Zheng, Y.-R.; Hemann, M. T.; Lippard, S. J. A Breast Cancer Stem Cell-Selective, Mammospheres-Potent Osmium(VI) Nitrido Complex. *J. Am. Chem. Soc.* **2014**, *135*, 14413−14416.
(37) Zou, T.; Lok, C.-N.; Fung, Y. M. E.; Che, C.-M. Luminescent Organoplatinum(II) Complexes Containing Bis(*N*-Heterocyclic Carbene) Ligands Selectively Target the Endoplasmic Reticulum and Induce Potent Photo-Toxicity. *Chem. Commun.* **2013**, *49*, 5423−5425.
(38) Wang, X.; Guo, Q.; Tao, L.; Zhao, L.; Chen, Y.; An, T.; Chen, Z.; Fu, R. E Platinum, a Newly Synthesized Platinum Compound, Induces Apoptosis through ROS-Triggered ER Stress in Gastric Carcinoma Cells. *Mol. Carcinog.* **2017**, *56*, 218−231.
(39) Ma, D. L.; Che, C. M.; Siu, F. M.; Yang, M.; Wong, K. Y. DNA Binding and Cytotoxicity of Ruthenium(II) and Rhenium(I) Complexes of 2-Amino-4-Phenylamino-6-(2-Pyridyl)-1,3,5-Triazine. *Inorg. Chem.* **2007**, *46*, 740−749.
(40) Viola-Villegas, N.; Rabideau, A. E.; Cesnavicious, J.; Zubieta, J.; Doyle, R. P. Targeting the Folate Receptor (FR): Imaging and Cytotoxicity of Re^{I} Conjugates in FR-Overexpressing Cancer Cells. *ChemMedChem* **2008**, *3*, 1387−1394.
(41) Fernández-Moreira, V.; Marzo, I.; Gimeno, M. C. Luminescent Re(I) and Re(I)/Au(I) Complexes as Cooperative Partners in Cell Imaging and Cancer Therapy. *Chem. Sci.* **2014**, *5*, 4434−4446.
(42) Collery, P.; Mohsen, A.; Kermagoret, A.; Corre, S.; Bastian, G.; Tomas, A.; Wei, M.; Santoni, F.; Guerra, N.; Desmaële, D.; D'Angelo, J. Antitumor Activity of a Rhenium(I)-Diselenoether Complex in Experimental Models of Human Breast Cancer. *Invest. New Drugs* **2015**, *33*, 848−860.
(43) Imstepf, S.; Pierroz, V.; Raposinho, P.; Bauwens, M.; Felber, M.; Fox, T.; Shapiro, A. B.; Freudenberg, R.; Fernandes, C.; Gama, S.; Gasser, G.; Motthagy, F.; Santos, I. R.; Alberto, R. Nuclear Targeting with an Auger Electron Emitter Potentiates the Action of a Widely Used Antineoplastic Drug. *Bioconjugate Chem.* **2015**, *26*, 2397−2407.
(44) Suntharalingam, K.; Awuah, S. G.; Bruno, P. M.; Johnstone, T. C.; Wang, F.; Lin, W.; Zheng, Y.-R.; Page, J. E.; Hemann, M. T.; Lippard, S. J. Necroptosis-Inducing Rhenium(V) Oxo Complexes. *J. Am. Chem. Soc.* **2015**, *137*, 2967−2974.
(45) Santoro, G.; Zlateva, T.; Ruggi, A.; Quaroni, L.; Zobi, F. Synthesis, Characterization and Cellular Location of Cytotoxic Constitutional Organometallic Isomers of Rhenium Delivered on a Cyanocobalmin Scaffold. *Dalton Trans.* **2015**, *44*, 6999−7008.
(46) Imstepf, S.; Pierroz, V.; Rubbiani, R.; Felber, M.; Fox, T.; Gasser, G.; Alberto, R. Organometallic Rhenium Complexes Divert Doxorubicin to the Mitochondria. *Angew. Chem., Int. Ed.* **2016**, *55*, 2792−2795.
(47) Ye, R.-R.; Tan, C.-P.; Chen, M.-H.; Hao, L.; Ji, L.-N.; Mao, Z.-W. Mono- and Dinuclear Phosphorescent Rhenium(I) Complexes: Impact of Subcellular Localization on Anticancer Mechanisms. *Chem. - Eur. J.* **2016**, *22*, 7800−7809.
(48) Simpson, P. V.; Casari, I.; Paternoster, S.; Skelton, B. W.; Falasca, M.; Massi, M. Defining the Anti-Cancer Activity of Tricarbonyl Rhenium Complexes: Induction of G2/M Cell Cycle Arrest and Blockade of Aurora-A Kinase Phosphorylation. *Chem. - Eur. J.* **2017**, *23*, 6518−6521.
(49) Mallick, S.; Ghosh, M. K.; Mandal, S.; Rane, V.; Kadam, R.; Chatterjee, A.; Bhattacharyya, A.; Chattopadhyay, S. The First Examples of Multiply Bonded Dirhenium(III,II) Paramagnetic Complexes Containing Nitrobenzoate Ligands: Spectroscopic, Structural, Cytotoxicity and Computational Studies. *Dalton Trans.* **2017**, *46*, 5670−5679.
(50) Luengo, A.; Fernández-Moreira, V.; Marzo, I.; Gimeno, M. C. Bioactive Heterobimetallic Re(I)/Au(I) Complexes Containing Bidentate N-Heterocyclic Carbenes. *Organometallics* **2018**, *37*, 3993−4001.
(51) Orsa, D. K.; Haynes, G. K.; Pramanik, S. K.; Iwunze, M. O.; Greco, G. E.; Ho, D. M.; Krause, J. A.; Hill, D. A.; Williams, R. J.; Mandal, S. K. The One-Pot Synthesis and the Fluorescence and Cytotoxicity Studies of Chlorotricarbonyl(α-Diimine)Rhenium(I), Fac-$(CO)_3$(α-Diimine)ReCl, Complexes. *Inorg. Chem. Commun.* **2008**, *11*, 1054−1056.
(52) Giffard, D.; Fischer-Fodor, E.; Vlad, C.; Achimas-Cadariu, P.; Smith, G. S. Synthesis and Antitumour Evaluation of Mono- and Multinuclear [2 + 1] Tricarbonylrhenium(I) Complexes. *Eur. J. Med. Chem.* **2018**, *157*, 773−781.
(53) Muñoz-Osses, M.; Godoy, F.; Fierro, A.; Gómez, A.; Metzler-Nolte, N. New Organometallic Imines of Rhenium(I) as Potential Ligands of GSK-3β: Synthesis, Characterization and Biological Studies. *Dalton Trans.* **2018**, *47*, 1233−1242.
(54) Wilder, P. T.; Weber, D. J.; Winstead, A.; Parnell, S.; Hinton, T. V.; Stevenson, M.; Giri, D.; Azemati, S.; Olczak, P.; Powell, B. V.; Odebode, T.; Tadesse, S.; Zhang, Y.; Pramanik, S. K.; Wachira, J. M.; Ghimire, S.; McCarthy, P.; Barfield, A.; Banerjee, H. N.; Chen, C.; Golen, J. A.; Rheingold, A. L.; Krause, J. A.; Ho, D. M.; Zavalij, P. Y.; Shaw, R.; Mandal, S. K. Unprecedented Anticancer Activities of Organorhenium Sulfonato and Carboxylato Complexes against Hormone-Dependent MCF-7 and Hormone-Independent Triple-Negative MDA-MB-231 Breast Cancer Cells. *Mol. Cell. Biochem.* **2018**, *441*, 151−163.
(55) Collery, P.; Desmaele, D.; Vijaykumar, V. Design of Rhenium Compounds in Targeted Anticancer Therapeutics. *Curr. Pharm. Des.* **2019**, *25*, 3306−3322.
(56) Bauer, E. B.; Haase, A. A.; Reich, R. M.; Crans, D. C.; Kühn, F. E. Organometallic and Coordination Rhenium Compounds and Their Potential in Cancer Therapy. *Coord. Chem. Rev.* **2019**, *393*, 79−117.
(57) Delasoie, J.; Pavic, A.; Voutier, N.; Vojnovic, S.; Crochet, A.; Nikodinovic-Runic, J.; Zobi, F. Highly Potent Rhenium(I) Tricarbonyl Complexes with Dual Anticancer and Anti-Angiogenic Activity Against Colorectal Carcinoma. *ChemRxiv* **2020**. DOI: 10.26434/CHEMRXIV.12012840.V2.
(58) Martínez-Lillo, J.; Mastropietro, T. F.; Lappano, R.; Madeo, A.; Alberto, M. E.; Russo, N.; Maggiolini, M.; De Munno, G. Rhenium(IV) Compounds Inducing Apoptosis in Cancer Cells. *Chem. Commun.* **2011**, *47*, 5283−5285.
(59) Choi, A. W.-T.; Louie, M.-W.; Li, S. P.-Y.; Liu, H.-W.; Chan, B. T.-N.; Lam, T. C.-Y.; Lin, A. C.-C.; Cheng, S.-H.; Lo, K. K.-W. Emissive Behavior, Cytotoxic Activity, Cellular Uptake, and PEGylation Properties of New Luminescent Rhenium(I) Polypyridine Poly(Ethylene Glycol) Complexes. *Inorg. Chem.* **2012**, *51*, 13289−13302.
(60) Mbagu, M. K.; Kebulu, D. N.; Winstead, A.; Pramanik, S. K.; Banerjee, H. N.; Iwunze, M. O.; Wachira, J. M.; Greco, G. E.; Haynes, G. K.; Sehmer, A.; Sarkar, F. H.; Ho, D. M.; Pike, R. D.; Mandal, S. K. Fac-Tricarbonyl(Pentylcarbonato)(α-Diimine)Rhenium Complexes: One-Pot Synthesis, Characterization, Fluorescence Studies, and Cytotoxic Activity against Human MDA-MB-231 Breast, CCl-227 Colon and BxPC-3 Pancreatic Carcinoma Cell Lines. *Inorg. Chem. Commun.* **2012**, *21*, 35−38.
(61) Clède, S.; Lambert, F.; Saint-Fort, R.; Plamont, M.-A.; Bertrand, H.; Vessières, A.; Policar, C. Influence of the Side-Chain Length on the Cellular Uptake and the Cytotoxicity of Rhenium

https://dx.doi.org/10.1021/acs.inorgchem.0c01442
Inorg. Chem. 2020, 59, 10285−10303

Triscarbonyl Derivatives: A Bimodal Infrared and Luminescence Quantitative Study. *Chem. - Eur. J.* **2014**, *20*, 8714−8722.
(62) Leonidova, A.; Pierroz, V.; Adams, L. A.; Barlow, N.; Ferrari, S.; Graham, B.; Gasser, G. Enhanced Cytotoxicity through Conjugation of a "Clickable" Luminescent Re(I) Complex to a Cell-Penetrating Lipopeptide. *ACS Med. Chem. Lett.* **2014**, *5*, 809−814.
(63) Leonidova, A.; Gasser, G. Underestimated Potential of Organometallic Rhenium Complexes as Anticancer Agents. *ACS Chem. Biol.* **2014**, *9*, 2180−2193.
(64) Leonidova, A.; Pierroz, V.; Rubbiani, R.; Heier, J.; Ferrari, S.; Gasser, G. Towards Cancer Cell-Specific Phototoxic Organometallic Rhenium(I) Complexes. *Dalton Trans.* **2014**, *43*, 4287−4294.
(65) Knopf, K. M.; Murphy, B. L.; MacMillan, S. N.; Baskin, J. M.; Barr, M. P.; Boros, E.; Wilson, J. J. In Vitro Anticancer Activity and in Vivo Biodistribution of Rhenium(I) Tricarbonyl Aqua Complexes. *J. Am. Chem. Soc.* **2017**, *139*, 14302−14314.
(66) Marker, S. C.; MacMillan, S. N.; Zipfel, W. R.; Li, Z.; Ford, P. C.; Wilson, J. J. Photoactivated in Vitro Anticancer Activity of Rhenium(I) Tricarbonyl Complexes Bearing Water-Soluble Phosphines. *Inorg. Chem.* **2018**, *57*, 1311−1331.
(67) Konkankit, C. C.; King, A. P.; Knopf, K. M.; Southard, T. L.; Wilson, J. J. In Vivo Anticancer Activity of a Rhenium(I) Tricarbonyl Complex. *ACS Med. Chem. Lett.* **2019**, *10*, 822−827.
(68) Konkankit, C. C.; Vaughn, B. A.; MacMillan, S. N.; Boros, E.; Wilson, J. J. Combinatorial Synthesis to Identify a Potent, Necrosis-Inducing Rhenium Anticancer Agent. *Inorg. Chem.* **2019**, *58*, 3895−3909.
(69) King, A. P.; Marker, S. C.; Swanda, R. V.; Woods, J. J.; Qian, S.; Wilson, J. J. A Rhenium Isonitrile Complex Induces Unfolded Protein Response-Mediated Apoptosis in Cancer Cells. *Chem. - Eur. J.* **2019**, *25*, 9206−9210.
(70) Konkankit, C. C.; Lovett, J.; Harris, H. H.; Wilson, J. J. X-Ray Fluorescence Microscopy Reveals That Rhenium(I) Tricarbonyl Isonitrile Complexes Remain Intact *in Vitro*. *Chem. Commun.* **2020**, *56*, 6515−6518.
(71) Marker, S. C.; King, A. P.; Swanda, R. V.; Vaughn, B.; Boros, E.; Qian, S.; Wilson, J. J. Exploring Ovarian Cancer Cell Resistance to Rhenium Anticancer Complexes. *Angew. Chem., Int. Ed.* **2020** DOI: 10.1002/anie.202004883.
(72) Stoyanov, S. R.; Villegas, J. M.; Cruz, A. J.; Lockyear, L. L.; Reibenspies, J. H.; Rillema, D. P. Computational and Spectroscopic Studies of Re(I) Bipyridyl Complexes Containing 2,6-Dimethylphenylisocyanide (CNx) Ligand. *J. Chem. Theory Comput.* **2005**, *1*, 95−106.
(73) Huynh, L.; Wang, Z.; Yang, J.; Stoeva, V.; Lough, A.; Manners, I.; Winnik, M. A. Evaluation of Phosphorescent Rhenium and Iridium Complexes in Polythionylphosphazene Films for Oxygen Sensor Applications. *Chem. Mater.* **2005**, *17*, 4765−4773.
(74) Villegas, J. M.; Stoyanov, S. R.; Moore, C. E.; Eichhorn, D. M.; Rillema, D. P. *fac*-Tricarbonyl(2,9-Dimethyl-1,10-Phenanthroline)-(2,6-Dimethylphenyl Isocyanide)Rhenium(I) Hexafluorophosphate. *Acta Crystallogr., Sect. E: Struct. Rep. Online* **2005**, *61*, m533−m534.
(75) Ko, C. C.; Ng, C. O.; Yiu, S. M. Luminescent Rhenium(I) Phenanthroline Complexes with a Benzoxazol-2-Ylidene Ligand: Synthesis, Characterization, and Photophysical Study. *Organometallics* **2012**, *31*, 7074−7084.
(76) Saleh, N.; Srebro, M.; Reynaldo, T.; Vanthuyne, N.; Toupet, L.; Chang, V. Y.; Muller, G.; Williams, J. A. G.; Roussel, C.; Autschbach, J.; Crassous, J. Enantio-Enriched CPL-Active Helicene-Bipyridine-Rhenium Complexes. *Chem. Commun.* **2015**, *51*, 3754−3757.
(77) Ugi, I. *Isonitrile Chemistry*; Academic Press: Cambdrige, MA, 1971.
(78) Bassett, J. M.; Berry, D. E.; Barker, G. K.; Green, M.; Howard, J. A. K.; Stone, F. G. A. Chemistry of Low-Valent Metal Isocyanide Complexes. Part 1. Synthesis of Zerovalent Iron and Ruthenium Complexes. Crystal and Molecular Structures of Tetrakis(t-Butyl Isocyanide)(Triphenylphosphine)Ruthenium and Pentakis(t-Butyl Isocyanide)Iron. *J. Chem. Soc., Dalton Trans.* **1979**, 1003−1011.
(79) Martin, G. E.; Hadden, C. E. Long-Range ^{1}H-^{15}N Heteronuclear Shift Correlation at Natural Abundance. *J. Nat. Prod.* **2000**, *63*, 543−585.
(80) Zou, T.; Sadler, P. J. Speciation of Precious Metal Anti-Cancer Complexes by NMR Spectroscopy. *Drug Discovery Today: Technol.* **2015**, *16*, 7−15.
(81) Pazderski, L.; Szłyk, E.; Sitkowski, J.; Kamieński, B.; Kozerski, L.; Toušek, J.; Marek, R. Experimental and Quantum-Chemical Studies of ^{15}N NMR Coordination Shifts in Palladium and Platinum Chloride Complexes with Pyridine, 2,2′-Bipyridine and 1,10-Phenanthroline. *Magn. Reson. Chem.* **2006**, *44*, 163−170.
(82) Romero-Canelón, I.; Sadler, P. J. Next-Generation Metal Anticancer Complexes: Multitargeting via Redox Modulation. *Inorg. Chem.* **2013**, *52*, 12276−12291.
(83) Zhang, P.; Sadler, P. J. Redox-Active Metal Complexes for Anticancer Therapy. *Eur. J. Inorg. Chem.* **2017**, *52*, 1541−1548.
(84) Ko, C.-C.; Lo, L. T.-L.; Ng, C.-O.; Yiu, S.-M. Photochemical Synthesis of Intensely Luminescent Isocyano Rhenium(I) Complexes with Readily Tunable Structural Features. *Chem. - Eur. J.* **2010**, *16*, 13773−13782.
(85) Lo, K. K.-W. Luminescent Rhenium(I) and Iridium(III) Polypyridine Complexes as Biological Probes, Imaging Reagents, and Photocytotoxic Agents. *Acc. Chem. Res.* **2015**, *48*, 2985−2995.
(86) Lee, L. C.-C.; Leung, K.-K.; Lo, K. K.-W. Recent Development of Luminescent Rhenium(I) Tricarbonyl Polypyridine Complexes as Cellular Imaging Reagents, Anticancer Drugs, and Antibacterial Agents. *Dalton Trans.* **2017**, *46*, 16357−16380.
(87) Favale, J. M.; Danilov, E. O.; Yarnell, J. E.; Castellano, F. N. Photophysical Processes in Rhenium(I) Diiminetricarbonyl Arylisocyanides Featuring Three Interacting Triplet Excited States. *Inorg. Chem.* **2019**, *58*, 8750−8762.
(88) Caspar, J. V.; Meyer, T. J. Application of the Energy Gap Law to Nonradiative, Excited-State Decay. *J. Phys. Chem.* **1983**, *87*, 952−957.
(89) Villegas, J. M.; Stoyanov, S. R.; Huang, W.; Rillema, D. P. Photophysical, Spectroscopic, and Computational Studies of a Series of Re(I) Tricarbonyl Complexes Containing 2,6-Dimethylphenylisocyanide and 5- and 6-Derivatized Phenanthroline Ligands. *Inorg. Chem.* **2005**, *44*, 2297−2309.
(90) Verma, R. P.; Hansch, C. Use of ^{13}C NMR Chemical Shift as QSAR/QSPR Descriptor. *Chem. Rev.* **2011**, *111*, 2865−2899.
(91) Tetko, I. V.; Gasteiger, J.; Todeschini, R.; Mauri, A.; Livingstone, D.; Ertl, P.; Palyulin, V. A.; Radchenko, E. V.; Zefirov, N. S.; Makarenko, A. S.; Tanchuk, V. Y.; Prokopenko, V. V. Virtual Computational Chemistry Laboratory - Design and Description. *J. Comput.-Aided Mol. Des.* **2005**, *19*, 453−463.
(92) VCCLAB. Virtual Computational Chemistry Laboratory http://www.vcclab.org.
(93) Wilson, J. J.; Lippard, S. J. In Vitro Anticancer Activity of Cis-Diammineplatinum(II) Complexes with β-Diketonate Leaving Group Ligands. *J. Med. Chem.* **2012**, *55*, 5326−5336.
(94) Fernández-Moreira, V.; Thorp-Greenwood, F. L.; Coogan, M. P. Application of d^6 Transition Metal Complexes in Fluorescence Cell Imaging. *Chem. Commun.* **2010**, *46*, 186−202.
(95) Zhao, Q.; Huang, C.; Li, F. Phosphorescent Heavy-Metal Complexes for Bioimaging. *Chem. Soc. Rev.* **2011**, *40*, 2508−2524.
(96) Gasser, G.; Neumann, S.; Ott, I.; Seitz, M.; Heumann, R.; Metzler-Nolte, N. Preparation and Biological Evaluation of Di-Hetero-Organometallic-Containing PNA Bioconjugates. *Eur. J. Inorg. Chem.* **2011**, *2011*, 5471−5478.
(97) Valente, A. J.; Maddalena, L. A.; Robb, E. L.; Moradi, F.; Stuart, J. A. A Simple ImageJ Macro Tool for Analyzing Mitochondrial Network Morphology in Mammalian Cell Culture. *Acta Histochem.* **2017**, *119*, 315−326.
(98) Beriault, D. R.; Werstuck, G. H. Detection and Quantification of Endoplasmic Reticulum Stress in Living Cells Using the Fluorescent Compound, Thioflavin T. *Biochim. Biophys. Acta, Mol. Cell Res.* **2013**, *1833*, 2293−2301.

https://dx.doi.org/10.1021/acs.inorgchem.0c01442
Inorg. Chem. 2020, 59, 10285−10303

(99) Vassar, P. S.; Culling, C. F. Fluorescent Stains, with Special Reference to Amyloid and Connective Tissues. *Arch. Pathol.* **1959**, *68*, 487−498.
(100) Biancalana, M.; Koide, S. Molecular Mechanism of Thioflavin-T Binding to Amyloid Fibrils. *Biochim. Biophys. Acta, Proteins Proteomics* **2010**, *1804*, 1405−1412.
(101) Chakrabarti, A.; Chen, A. W.; Varner, J. D. A Review of the Mammalian Unfolded Protein Response. *Biotechnol. Bioeng.* **2011**, *108*, 2777−2793.
(102) Hetz, C. The Unfolded Protein Response: Controlling Cell Fate Decisions under ER Stress and Beyond. *Nat. Rev. Mol. Cell Biol.* **2012**, *13*, 89−102.
(103) Adams, C. J.; Kopp, M. C.; Larburu, N.; Nowak, P. R.; Ali, M. M. U. Structure and Molecular Mechanism of ER Stress Signaling by the Unfolded Protein Response Signal Activator IRE1. *Front. Mol. Biosci.* **2019**, *6*, 11.
(104) Matsumoto, H.; Miyazaki, S.; Matsuyama, S.; Takeda, M.; Kawano, M.; Nakagawa, H.; Nishimura, K.; Matsuo, S. Selection of Autophagy or Apoptosis in Cells Exposed to ER-Stress Depends on ATF4 Expression Pattern with or without CHOP Expression. *Biol. Open* **2013**, *2*, 1084−1090.
(105) Schmidt, E. K.; Clavarino, G.; Ceppi, M.; Pierre, P. SUnSET, a Nonradioactive Method to Monitor Protein Synthesis. *Nat. Methods* **2009**, *6*, 275−277.
(106) Akbar, M. U.; Ahmad, M. R.; Shaheen, A.; Mushtaq, S. A Review on Evaluation of Technetium-99m Labeled Radiopharmaceuticals. *J. Radioanal. Nucl. Chem.* **2016**, *310*, 477−493.
(107) Boschi, A.; Uccelli, L.; Martini, P. A Picture of Modern Tc-99m Radiopharmaceuticals: Production, Chemistry, and Applications in Molecular Imaging. *Appl. Sci.* **2019**, *9*, 2526.
(108) Nunes, P.; Morais, G. R.; Palma, E.; Silva, F.; Oliveira, M. C.; Ferreira, V. F. C.; Mendes, F.; Gano, L.; Miranda, H. V.; Outeiro, T. F.; Santos, I.; Paulo, A. Isostructural Re(I)/^{99m}Tc(I) Tricarbonyl Complexes for Cancer Theranostics. *Org. Biomol. Chem.* **2015**, *13*, 5182−5194.
(109) North, A. J.; Hayne, D. J.; Schieber, C.; Price, K.; White, A. R.; Crouch, P. J.; Rigopoulos, A.; OKeefe, G. J.; Tochon-Danguy, H.; Scott, A. M.; White, J. M.; Ackermann, U.; Donnelly, P. S. Toward Hypoxia-Selective Rhenium and Technetium Tricarbonyl Complexes. *Inorg. Chem.* **2015**, *54*, 9594−9610.
(110) Baumeister, J. E.; Reinig, K. M.; Barnes, C. L.; Kelley, S. P.; Jurisson, S. S. Technetium and Rhenium Schiff Base Compounds for Nuclear Medicine: Syntheses of Rhenium Analogues to ^{99m}Tc-Furifosmin. *Inorg. Chem.* **2018**, *57*, 12920−12933.
(111) Barbarics, E.; Kronauge, J. F.; Costello, C. E.; Jànokp, G. A.; Holman, B. L.; Davison, A.; Jones, A. G. In Vivo Metabolism of the Technetium Isonitrile Complex [Tc(2-Ethoxy-2-Methyl-1-Isocyanopropane)$_6$]$^+$. *Nucl. Med. Biol.* **1994**, *21*, 583−591.
(112) Pietzsch, H. J.; Gupta, A.; Syhre, R.; Leibnitz, P.; Spies, H. Mixed-Ligand Technetium(III) Complexes with Tetradendate/Monodendate NS$_3$/Isocyanide Coordination: A New Nonpolar Technetium Chelate System for the Design of Neutral and Lipophilic Complexes Stable in Vivo. *Bioconjugate Chem.* **2001**, *12*, 538−544.
(113) Zhang, X. Z.; Wang, X. B.; Zhou, J. M. A New Technetium-99m Labeled Isonitrile Complex ^{99m}Tc-TMCHI as a Potential Blood Pool Imaging Agent. *Appl. Radiat. Isot.* **2003**, *59*, 231−235.
(114) Fuks, L.; Gniazdowska, E.; Kozminski, P.; Lyczko, M.; Mieczkowski, J.; Narbutt, J. 2 + 1" Tricarbonyltechnetium(I) and -Rhenium(I) Mixed-Ligand Complexes with N-Methylpyridine-2-Carboxyamide and Isocyanide or Imidazole Ligands-Potential Precursors of Radiopharmaceuticals. *Appl. Radiat. Isot.* **2010**, *68*, 90−95.
(115) Hayes, T. R.; Powell, A. S.; Barnes, C. L.; Benny, P. D. Synthesis and Stability of 2 + 1 Complexes of N,N-Diethylbenzoylthiourea with [MI(CO)$_3$]$^+$ (M = Re, ^{99m}Tc). *J. Coord. Chem.* **2015**, *68*, 3432−3448.
(116) Mizuno, Y.; Uehara, T.; Hanaoka, H.; Endo, Y.; Jen, C. W.; Arano, Y. Purification-Free Method for Preparing Technetium-99m-Labeled Multivalent Probes for Enhanced in Vivo Imaging of Saturable Systems. *J. Med. Chem.* **2016**, *59*, 3331−3339.
(117) Alberto, R.; Schibli, R.; Egli, A.; Schubiger, A. P.; Abram, U.; Kaden, T. A. A Novel Organometallic Aqua Complex of Technetium for the Labeling of Biomolecules: Synthesis of [^{99m}Tc(OH$_2$)$_3$(CO)$_3$]$^+$ from [^{99m}TcO$_4$]$^-$ in Aqueous Solution and Its Reaction with a Bifunctional Ligand. *J. Am. Chem. Soc.* **1998**, *120*, 7987−7988.
(118) Yazdani, A.; Janzen, N.; Banevicius, L.; Czorny, S.; Valliant, J. F. Imidazole-Based [2 + 1] Re(I)/^{99m}Tc(I) Complexes as Isostructural Nuclear and Optical Probes. *Inorg. Chem.* **2015**, *54*, 1728−1736.
(119) Baggish, A. L.; Boucher, C. A. Radiopharmaceutical Agents for Myocardial Perfusion Imaging. *Circulation* **2008**, *118*, 1668−1674.
(120) Manabe, O.; Kikuchi, T.; Scholte, A. J. H. A.; El Mahdiui, M.; Nishii, R.; Zhang, M.-R.; Suzuki, E.; Yoshinaga, K. Radiopharmaceutical Tracers for Cardiac Imaging. *J. Nucl. Cardiol.* **2018**, *25*, 1204−1236.
(121) Ellis, B. L.; Gorshkov, N. I.; Lumpov, A. A.; Miroslavov, A. E.; Yalfimov, A. N.; Gurzhiy, V. V.; Suglobov, D. N.; Braddock, R.; Adams, J. C.; Smith, A.-M.; Prescott, M. C.; Sharma, H. L. Synthesis, Characterization and Pre-Clinical Evaluation of ^{99m} Tc-Tricarbonyl Complexes as Potential Myocardial Perfusion Imaging Agents. *J. Labelled Compd. Radiopharm.* **2013**, *56*, 700−707.
(122) Liu, X.; Jiang, C.; Li, Y.; Liu, W.; Yao, N.; Gao, M.; Ji, Y.; Huang, D.; Yin, Z.; Sun, Z.; Ni, Y.; Zhang, J. Evaluation of Hypericin: Effect of Aggregation on Targeting Biodistribution. *J. Pharm. Sci.* **2015**, *104*, 215−222.
(123) Yang, L.; Kuang, H.; Zhang, W.; Aguilar, Z. P.; Wei, H.; Xu, H. Comparisons of the Biodistribution and Toxicological Examinations after Repeated Intravenous Administration of Silver and Gold Nanoparticles in Mice. *Sci. Rep.* **2017**, *7*, 3303.
(124) Waegeneers, N.; Brasseur, A.; Van Doren, E.; Van der Heyden, S.; Serreyn, P. J.; Pussemier, L.; Mast, J.; Schneider, Y. J.; Ruttens, A.; Roels, S. Short-Term Biodistribution and Clearance of Intravenously Administered Silica Nanoparticles. *Toxicol. Reports* **2018**, *5*, 632−638.
(125) Meier-Menches, S. M.; Gerner, C.; Berger, W.; Hartinger, C. G.; Keppler, B. K. Structure-Activity Relationships for Ruthenium and Osmium Anticancer Agents-towards Clinical Development. *Chem. Soc. Rev.* **2018**, *47*, 909−928.
(126) He, L.; Pan, Z. Y.; Qin, W. W.; Li, Y.; Tan, C. P.; Mao, Z. W. Impairment of the Autophagy-Related Lysosomal Degradation Pathway by an Anticancer Rhenium(I) Complex. *Dalton Trans.* **2019**, *48*, 4398−4404.
(127) Wang, F. X.; Liang, J. H.; Zhang, H.; Wang, Z. H.; Wan, Q.; Tan, C. P.; Ji, L. N.; Mao, Z. W. Mitochondria-Accumulating Rhenium(I) Tricarbonyl Complexes Induce Cell Death via Irreversible Oxidative Stress and Glutathione Metabolism Disturbance. *ACS Appl. Mater. Interfaces* **2019**, *11*, 13123−13133.
(128) Capper, M. S.; Rehkämper, M.; Packman, H. Rhenium-Based Complexes and in Vivo Testing: A Brief History. *ChemBioChem* **2020**. DOI: 10.1002/cbic.202000117.
(129) Gramatica, P.; Papa, E.; Luini, M.; Monti, E.; Gariboldi, M. B.; Ravera, M.; Gabano, E.; Gaviglio, L.; Osella, D. Antiproliferative Pt(IV) Complexes: Synthesis, Biological Activity, and Quantitative Structure-Activity Relationship Modeling. *JBIC, J. Biol. Inorg. Chem.* **2010**, *15*, 1157−1169.
(130) Varbanov, H. P.; Jakupec, M. A.; Roller, A.; Jensen, F.; Galanski, M.; Keppler, B. K. Theoretical Investigations and Density Functional Theory Based Quantitative Structure-Activity Relationships Model for Novel Cytotoxic Platinum(IV) Complexes. *J. Med. Chem.* **2013**, *56*, 330−344.
(131) Gutiérrez, A.; Gracia-Fleta, L.; Marzo, I.; Cativiela, C.; Laguna, A.; Gimeno, M. C. Gold(I) Thiolates Containing Amino Acid Moieties. Cytotoxicity and Structure-Activity Relationship Studies. *Dalton Trans.* **2014**, *43*, 17054−17066.
(132) Yellol, J.; Pérez, S. A.; Buceta, A.; Yellol, G.; Donaire, A.; Szumlas, P.; Bednarski, P. J.; Makhloufi, G.; Janiak, C.; Espinosa, A.; Ruiz, J. Novel C,N-Cyclometalated Benzimidazole Ruthenium(II)

and Iridium(III) Complexes as Antitumor and Antiangiogenic Agents: A Structure-Activity Relationship Study. *J. Med. Chem.* **2015**, *58*, 7310−7327.
(133) Tabrizi, L.; Chiniforoshan, H. Designing New Iridium(III) Arene Complexes of Naphthoquinone Derivatives as Anticancer Agents: A Structure-Activity Relationship Study. *Dalton Trans.* **2017**, *46*, 2339−2349.
(134) Chow, M. J.; Licona, C.; Pastorin, G.; Mellitzer, G.; Ang, W. H.; Gaiddon, C. Structural Tuning of Organoruthenium Compounds Allows Oxidative Switch to Control ER Stress Pathways and Bypass Multidrug Resistance. *Chem. Sci.* **2016**, *7*, 4117−4124.
(135) Li, C.; Ip, K.-W.; Man, W.-L.; Song, D.; He, M.-L.; Yiu, S.-M.; Lau, T.-C.; Zhu, G. Cytotoxic (Salen)Ruthenium(III) Anticancer Complexes Exhibit Different Modes of Cell Death Directed by Axial Ligands. *Chem. Sci.* **2017**, *8*, 6865−6870.
(136) Kurz, P.; Probst, B.; Spingler, B.; Alberto, R. Ligand Variations in [ReX(Diimine)$(CO)_3$] Complexes: Effects on Photocatalytic CO_2 Reduction. *Eur. J. Inorg. Chem.* **2006**, 2966−2974.
(137) Smieja, J. M.; Kubiak, C. P. Re(Bipy-tBu)$(CO)_3$Cl−Improved Catalytic Activity for Reduction of Carbon Dioxide: IR-Spectroelectrochemical and Mechanistic Studies. *Inorg. Chem.* **2010**, *49*, 9283−9289.
(138) Yuan, Y.; Dong, W.; Gao, X.; Gao, H.; Xie, X.; Zhang, Z. Visible-Light-Induced Radical Cascade Cyclization: Synthesis of the ABCD Ring Cores of Camptothecins. *J. Org. Chem.* **2018**, *83*, 2840−2846.
(139) *CrysAlisPro*. Rigaku OD: The Woodlands, TX, 2015.
(140) Sheldrick, G. M. SHELXT - Integrated Space-Group and Crystal-Structure Determination. *Acta Crystallogr., Sect. A: Found. Adv.* **2015**, *71*, 3−8.
(141) Sheldrick, G. M. Crystal Structure Refinement with SHELXL. *Acta Crystallogr., Sect. C: Struct. Chem.* **2015**, *71*, 3−8.
(142) Müller, P. Practical Suggestions for Better Crystal Structures. *Crystallogr. Rev.* **2009**, *15*, 57−83.
(143) Brouwer, A. M. Standards for Photoluminescence Quantum Yield Measurements in Solution (IUPAC Technical Report). *Pure Appl. Chem.* **2011**, *83*, 2213−2228.

https://dx.doi.org/10.1021/acs.inorgchem.0c01442
Inorg. Chem. 2020, 59, 10285−10303